WAKE DISSIPATION AND TOTAL PRESSURE LOSS IN A TWO-DIMENSIONAL COMPRESSOR CASCADE WITH CRENULATED TRAILING EDGES

THESIS

Janet Lyle Veesart
First Lieutenant

AFIT/GAE/ENY/89J-3

DEPARTMENT OF THE AIR FORCE
AIR UNIVERSITY
AIR FORCE INSTITUTE OF TECHNOLOGY
Wright-Patterson Air Force Base, Ohio

AFIT/GAE/ENY/89J-3

WAKE DISSIPATION AND TOTAL PRESSURE LOSS IN A TWO-DIMENSIONAL COMPRESSOR CASCADE WITH CRENULATED TRAILING EDGES

THESIS

Janet Lyle Veesart
First Lieutenant

AFIT/GAE/ENY/89J-3

AFIT/GAE/ENY/89J-3

WAKE DISSIPATION AND TOTAL PRESSURE LOSS IN A TWO-DIMENSIONAL COMPRESSOR CASCADE WITH CRENULATED TRAILING EDGES

THESIS

Presented to the Faculty of the School of Engineering

of the Air Force Institute of Technology

Air University

In Partial Fulfillment of the

Requirements for the Degree of

Master of Science in Aeronautical Engineering

Janet Lyle Veesart, B.S.

First Lieutenant

June, 1989

Acknowledgments

Completion of this masters thesis is the culmination of a great deal of time and effort and would not have been possible without the support and encouragement of many people. I would like to thank my advisor, Lt Col Paul King, and my thesis committee members, Dr William Elrod, Dr Arthur Wennerstrom, and Captain James Planeaux for their indispensible guidance and advice throughout this project. Thanks also go to lab technicians Mr Dan Rioux, Mr Jay Anderson, Mr Mark Derriso, and Mr Tim Major for their help in keeping the "shark tank" up and running. Mr John Brohas of the AFIT Model Shop did an outstanding job modifying the test section to suit my needs and fabricating the unique equipment required by my research effort. A special thanks to my good friend Lt Mary Manning for her assistance in preparing this manuscript and her encouragement throughout this endeavor. And finally, a heartfelt thanks to my husband, Mike, for his support and understanding during my time at AFIT.

Yes, Mike, the thesis is finally finished.

Janet Lyle Veesart

Table of Contents

List of Figures

List of Tables

List of Symbols

Symbol	
A	calibration constant, heat transfer area (wetted area: πdl) (ft^2)
a	distance from leading edge to point of minimum camber (in)
B	calibration constant
b	calibration exponent
C	calibration constant
c	blade chord (in)
C_p	specific heat (0.240 Btu/(lbm-°R))
d	diameter (ft)
E	voltage (volts)
e'	voltage fluctuation (volts)
E_o	bridge voltage (volts)
E_w	voltage across hot wire sensor (volts)
E_3	voltage across series resistor (volts)
e_{rms}	root mean square voltage fluctuation (volts)
g_c	32.2 (lbm-ft)/(lbf-s^2)
h	film coefficient of heat transfer (Btu/(s-ft^2-°R))
i	incidence angle (deg)
I_w	sensor current (amps)
J	conversion factor (778.17 (ft-lbf)/Btu)
K	fluid thermal conductivity (Btu/(ft-s-°R))
K_o	reference fluid thermal conductivity (for $T_o = 492°R$, $K_o = 3.889 \times 10^{-6}$ Btu/(ft-s-°R))
K_1	calibration constant
K_2	calibration constant
K_3	calibration constant
l	sensor length (ft)
n	calibration constant
N_u	Nusselt number
P	total pressure (lb/in^2)
$\overline{P_A}$	area-averaged total pressure (lb/in^2)
P_o	reference total pressure (lb/in^2)
$\Delta\overline{P_A}$	area-averaged total pressure defect (lb/in^2)
$\overline{P_M}$	mass-averaged total pressure (lb/in^2)
$\Delta\overline{P_M}$	mass-averaged total pressure defect (lb/in^2)
P_s	static pressure (lb/in^2)
R	gas constant (for air, R = 53.36 (ft-lbf)/(°R-lbm)
R_{misc}	resistance due to probe support and holder, and anemometer cables (ohms)
R_W	resistance across sensor (ohms)
R_3	resistance across series resistor (ohms)
r_c	recovery factor
Re	Reynolds number

Symbol	
S_1	Sutherland's Law constant (for air, S_1=198°R)
s	blade spacing (in)
T	temperature (°R)
T_{AW}	adiabatic wall temperature (°R)
T_f	fluid temperature (°R)
T_m	Eckert mean temperature (°R)
T_o	reference total temperature (°R)
T_u	turbulence intensity
T_w	sensor temperature (°R)
U_{eff}	velocity normal to the sensor (ft/s)
$\overline{U}_{MEAN}$	flow velocity vector (ft/s)
U_{MEAN_X}	component of $\overline{U}_{MEAN}$ in X direction (ft/s)
U_{MEAN_Y}	component of $\overline{U}_{MEAN}$ in Y direction (ft/s)
$\overline{U}_{M1}$	component of $\overline{U}_{MEAN}$ normal to sensor #1 (ft/s)
$\overline{U}_{M2}$	component of $\overline{U}_{MEAN}$ normal to sensor #2 (ft/s)
$\overline{U}_{M1B}$	component of $\overline{U}_{MEAN}$ parallel to sensor #1 (ft/s)
$\overline{U}_{M2B}$	component of $\overline{U}_{MEAN}$ parallel to sensor #2 (ft/s)
U_N	component of flow velocity parallel to sensor (ft/s)
U_{NX}	X component of velocity parallel to sensor (ft/s)
U_{NY}	Y component of velocity parallel to sensor (ft/s)
U_X	X component of velocity normal to sensor (ft/s)
U_Y	Y component of velocity normal to sensor (ft/s)
u'	velocity fluctuation normal to the sensor (ft/s)
$\overline{u}$	time-averaged velocity fluctuation in the X direction (ft/s)
u_{rms}	root mean square velocity fluctuation (ft/s)
V	velocity (ft/s)
V_{cal}	flow velocity exiting the calibrator (ft/s)
$\overline{V_M}$	mass-averaged velocity (ft/s)
V_o	reference velocity (ft/s)
$\overline{v}$	time-averaged velocity fluctuation in the Y direction (ft/s)
V_1	air inlet velocity (ft/s)
V_2	air outlet velocity (ft/s)
V_X	X-component of velocity (ft/s)
V_Y	Y-component of velocity (ft/s)
V_Z	Z-component of velocity (ft/s)
$\overline{w}$	time-averaged velocity fluctuation in the Z direction (ft/s)
X	test section X axis
X_B	bisector reference frame X axis
X_{PS}	probe support reference frame X axis
X_{TS}	test section X axis
Y	test section Y axis
Y_B	bisector reference frame Y axis
Y_{PS}	probe support reference frame Y axis
Y_{TS}	text section Y axis

Symbol	
Z	text section Z axis
α	bisector angle (deg)
α_1	air inlet angle (deg), angle between probe bisector and sensor #1 (deg)
α_2	air outlet angle (deg), angle between probe bisector and sensor #2 (deg)
α_1'	blade inlet angle (deg), angle between the flow velocity and sensor #1 (deg)
α_2'	blade outlet angle (deg), angle between the flow velocity and sensor #2 (deg)
β	angle between probe support centerline and the test section X axis (deg)
δ	deviation angle (deg)
δ_y	wake width (in)
ϵ	deflection angle (deg)
γ	correction factor for probe misalignment $(\theta/2 + \beta)$ (deg)
π	pi
$\overline{\omega}$	total pressure loss coefficient
ρ	density (lbm/ft^3)
ρ_o	reference density (lbm/ft^3)
μ	viscosity (lbm/(ft-s))
μ_o	reference viscosity (for $T_o = 492°R$, $\mu_o = 1.173 \times 10^{-5}$ lbm/(ft-sec))
θ	blade camber angle (deg), offset angle (deg)
σ	relative turbulence
ζ	stagger angle (deg)

Abstract

Wake dissipation and total pressure loss in a two-dimensional, subsonic, compressor cascade with crenulated trailing edges were investigated in the Air Force Institute of Technology Cascade Test Facility. Three blade configurations, a baseline NACA 64-905 airfoil and two crenulated trailing edge patterns were used. Hot wire anemometry and a total pressure rake were used to collect the flow data. The smaller crenulation configuration exhibited the greatest turning angle and the least total pressure losses. The most rapid wake dissipation was generated by the larger crenulations' counterrotating vortices accompanied by slightly higher pressure losses than those created by the small crenulations. Both crenulated blade configurations had better wake dissipation, increased turning angles, and smaller pressure loss coefficients than the uncrenulated baseline blade.

WAKE DISSIPATION AND TOTAL PRESSURE LOSS IN A TWO-DIMENSIONAL COMPRESSOR CASCADE WITH CRENULATED TRAILING EDGES

I. Introduction

In the highly competitive world of aircraft gas turbine engines, engine weight is a critical design parameter. Any reduction in weight due to new materials or new designs translates directly into improved performance and decreased fuel consumption. In current axial compressor design, the number of vane rows and the number of vanes per row are conservatively chosen in order to prevent separation of the flow due to excessive turning and to avoid excessive aerodynamic blade loading. If a method of re-energizing the wake generated by the vanes could be developed, it would reduce the possibility of flow separation (20:1). Additionally, by increasing the diffusion rate of the fluid exiting the compressor, the diffuser leading to the combustor could be shortened, resulting in additional weight and length savings.

Trailing edge crenulations present one possible way of increasing wake re-energization. In this method, proposed by Dr Arthur J. Wennerstrom of the Wright Research and Development Center Aeropropulsion and Power Laboratory, a series of crenulations are made spanwise along the blade trailing edge as shown in Figure 1.1. Due to the pressure differential existing between the pressure and suction sides of the blade, the crenulations act as small vortex generators. The introduction of these counterrotating vortices into the exit flowfield of a compressor should increase the intermixing between the freestream flow and the fluid in the lower momentum wake region. Increased intermixing accelerates the dissipation of the fluid wakes and reduces the distance required to reach fully mixed out flow.

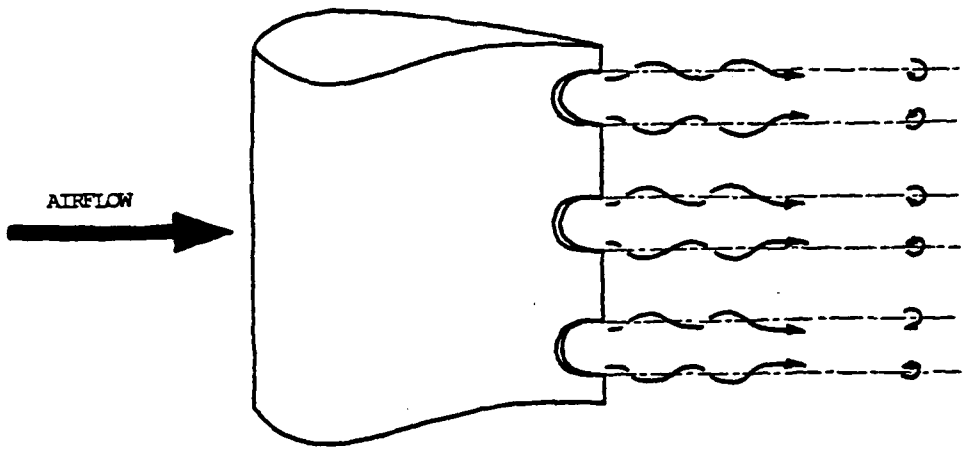

Figure 1.1. Crenulated Blade

Before this method can be of much use to the designer, the effects of these crenulated airfoils on the airflow must be quantified. The fully three-dimensional fluid environment of a compressor is extremely complex, and researchers have found the two-dimensional cascade to be a practical testbed for gaining information on the performance of new airfoil designs.

The objective of this research project was to investigate the effects of trailing edge crenulations on the exit flowfield in a two-dimensional cascade. The performance of three blade configurations, one uncrenulated baseline and two different crenulation patterns were studied. Total pressure loss and flow turning angle were the selected indicators of blade performance, while mass-averaged velocity deficit was used to quantify wake dissipation. Pressure and velocity profiles provided a qualitative picture of the various flowfield effects.

II. Cascade Aerodynamics

Blade Wake

When an airfoil is placed in a flow stream, viscous effects retard the flow of fluid adjacent to the blade's surface. As the distance from the blade surface increases, the viscous effects diminish and the fluid velocity rapidly approaches the freestream velocity. This region of low momentum fluid is known as the boundary layer. Although typically of very small dimensions, the boundary layer significantly influences the pressure distribution on the blade and in the flowfield downstream of the trailing edge. In addition, the pressure distribution along the blade, due to its curvature, affects the rate of boundary layer growth, particularly on the suction surface. As the flow proceeds down the blade, the boundary layers continue to grow. Once at the trailing edge, the boundary layers combine to form a blade wake, as shown in Figure 2.1 (adapted from (16:158)). This wake, formed by low momentum fluid, creates a local defect in total pressure.

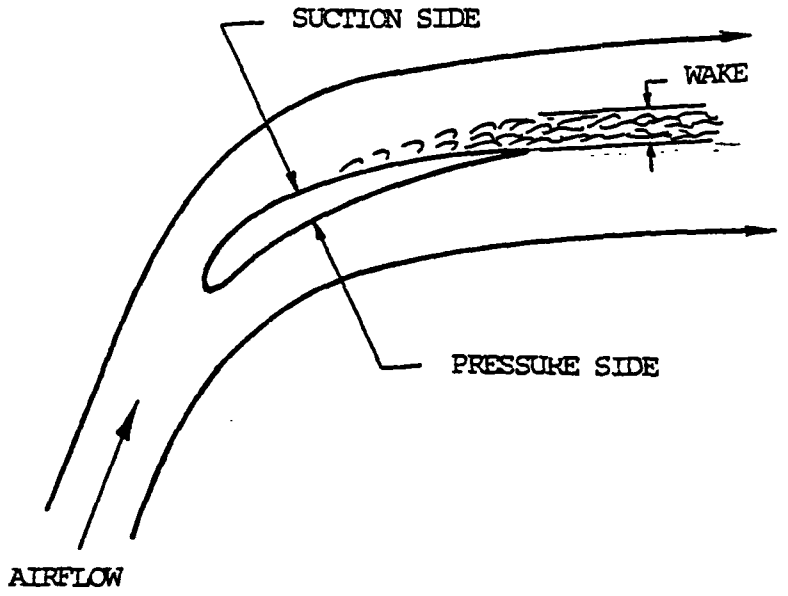

Figure 2.1. Blade Wake

Typical velocity and pressure profiles across a wake are shown in Figures 2.2 and 2.3 (adapted from (12:34)). The edge of the wake for both pressure and velocity measurements is normally defined to be the point in the wake profile where the flow attains 99.5% of the

freestream velocity (12:15). The width of the wake is denoted as δ_y and $\overline{P_M}$ represents the mass-averaged total pressure across one blade spacing defined by

$$\overline{P_M} = \frac{\int_{-s/2}^{s/2} \rho V_x P \, dy}{\int_{-s/2}^{s/2} \rho V_x \, dy} \qquad 2-1$$

The thicker the boundary layers at the trailing edge, the larger the blade wake.

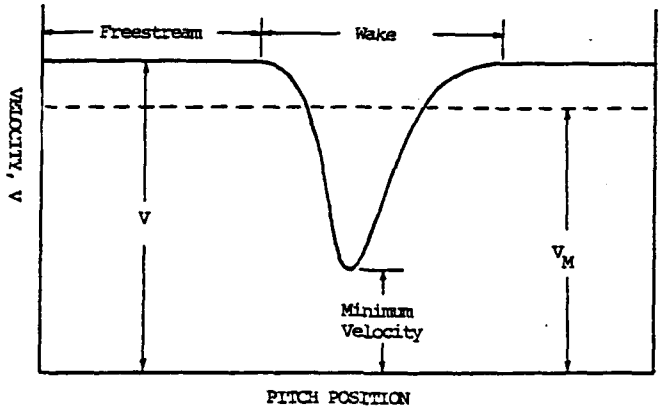

Figure 2.2. Velocity Profile Across a Wake

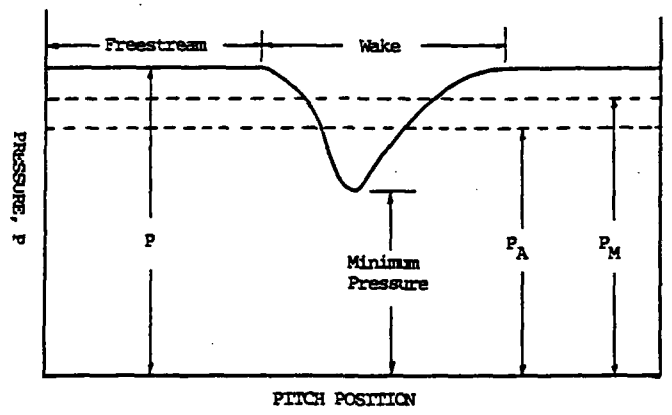

Figure 2.3. Pressure Profile across a Wake

Downstream of the trailing edge, the lower momentum fluid mixes with the higher velocity freestream flow. Total pressure losses accompany this mixing until the flow conditions again become uniform. The difference between the inlet total pressure and the total

pressure in this mixed out region of the flow is called the mixing loss and represents the entire total pressure loss of a given wake profile for two-dimensional cascade flow (13:4).

Cascade Losses

When a series of blades are combined to form a cascade, a similar pattern of wake development occurs, as shown in Figure 2.4 (13:34).

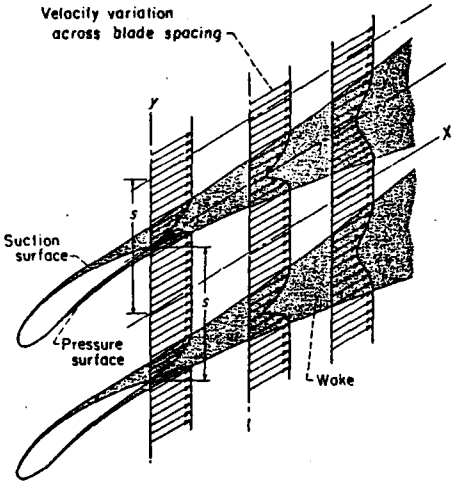

Figure 2.4. Cascade Wake

Evaluation of the flow losses through the cascade can be made using a variety of parameters such as drag coefficient, wake coefficient, total-pressure defect, or entropy rise (13:5). A widely used performance parameter is the total pressure loss coefficient, $\overline{\omega}$, defined as follows: (16:201)

$$\overline{\omega}_{ref} = \frac{\Delta\overline{P_M}}{(P_o - P_s)_{ref}} \qquad 2-2$$

where

$\Delta\overline{P_M} \equiv$ mass-averaged loss in total pressure across the cascade (see equation 2-6).

$(P_o - P_s)_{ref} \equiv$ Reference freestream dynamic pressure

For incompressible flow,

$$(P_o - P_s)_{ref} = \frac{1}{2}\rho_o V_o^2 \qquad 2-3$$

Many of the equations and relationships used to analyze the flow characteristics of the two-dimensional cascade come directly from the work of Lieblein and Roudebush (12:5,20). In their analysis of the low speed wake characteristics in two-dimensional cascades, they make the following flow assumptions.

1) The flow is two-dimensional and incompressible.

2) Static pressure and flow angle are constant across the entire blade spacing.

3) Inlet flow is uniform across the blade spacing.

4) The outlet total pressure is constant in the freestream outside the wake.

5) The outlet freestream total-pressure is equal to the inlet total pressure.

These assumptions permit the following derivations of area-averaged total pressure loss, mass-averaged total pressure loss, and mass-averaged velocity. Mass-averaging a property over the blade spacing provides a weighted average value based on the fluid's mass flow distribution. Note that these equations apply to a plane normal to the axial direction. The reference frame used is shown in Figure 2.5.

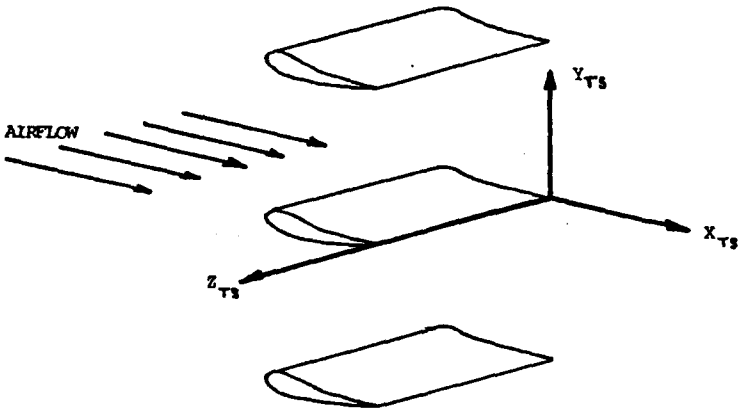

Figure 2.5. Cascade Reference Frame

Area-Averaged Total Pressure Defect ($\Delta\overline{P_A}$) (12:26)

$$\Delta\overline{P_A} = \frac{1}{s}\int_{-s/2}^{s/2} (P_o - P)\, dy \qquad 2-4$$

Applying Bernoulli's equation permits conversion to velocity terms

$$\Delta\overline{P_A} = \frac{1}{s}\int_{-s/2}^{s/2} \frac{\rho}{2}\left(V_o{}^2 - V^2\right) dy \qquad 2-5$$

Mass-Averaged Total Pressure Defect ($\Delta\overline{P_M}$) (12:26)

$$\Delta\overline{P_M} = \frac{\int_{-s/2}^{s/2} \rho V_x (P_o - P)\, dy}{\int_{-s/2}^{s/2} \rho V_x\, dy} \qquad 2-6$$

Mass-Averaged Velocity ($\overline{V_M}$)

$$\overline{V_M} = \frac{\int_{-s/2}^{s/2} \rho V_x (V)\, dy}{\int_{-s/2}^{s/2} \rho V_x\, dy} \qquad 2-7$$

Two-Dimensional Flow Considerations

In order for cascade data to be independent of the specific cascade used for the flow investigation, the flow must be two-dimensional. The following are among the criteria Erwin and Emery proposed for two-dimensional flow (8:2):

1) Equal pressures, velocities, and directions exist at different spanwise locations.
2) No regions of low-energy flow other than blade wake exists. The blade wakes are uniform in the spanwise direction.
3) The various performance values do not change with aspect ratio, number of blades, or other physical factors of the tunnel configuration.

Another indicator of the two-dimensionality of the flow in a cascade is the Axial Velocity Density Ratio (AVDR) defined by (9:40)

$$AVDR = \frac{\int_o^s \rho V_x \, dy}{\int_o^s \rho_o V_{x_o} \, dy} \qquad 2-8$$

According to Scholz (18:489), quasi-two-dimensional flow can be assumed to exist when $0.8 \leq AVDR \leq 1.2$.

III. Experimental Apparatus

Test Rig

The Air Force Institute of Technology (AFIT) Cascade Test Facility (CTF) was built in 1981 under the sponsorship of the Wright Aeronautical Laboratories Aero-Propulsion Laboratory and the Air Force Office of Scientific Research to provide a testbed for compressor cascade investigations. A schematic of the CTF is shown in Figure 3.1.

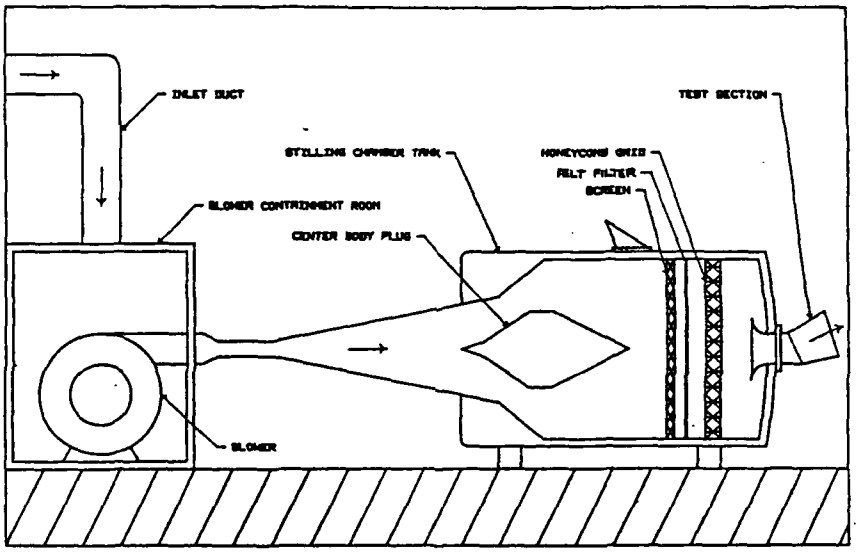

Figure 3.1. Cascade Facility

Airflow to the test section can be supplied by a 40 horsepower centrifugal blower or by a high pressure augmentor/ejector. These two sources can be used separately or in tandem. Individually, each airflow source creates approximately 40″ H_2O of total tank pressure, and coupled together tank total pressures as high as 95″ H_2O can be attained. (2:3-4). In the current study, only the centrifugal blower, rated at 3000 cubic feet per minute at 26 inches of head, was used.

The blower draws air in from outside the building through a 12 inch diameter duct. The air passes through a coarse mesh screen, intermixes with the warm laboratory air, and is electrostatically filtered in the blower containment room before entering the 9 foot

long diffusing section. The diffusing section slows the airflow down to about 20 ft/s and directs it into the stilling chamber. A foam-covered center body in the stilling chamber radially diffuses the airflow to approximately 10 ft/s. The air passes through a 40 mesh screen, a cloth filter, and a 4 inch thick honeycomb grid for final filtering and straightening before entering a standard ASME long radius bellmouth. The air exits the bellmouth at approximately 440 ft/s when the test section is not attached. With the test section in place, inlet airflows typically reach speeds of 508 ft/s. The airflow exhausts into the open laboratory. Laboratory temperatures range from 90°F (winter months) to well over 100°F (summer months) and vary from day to day based on atmospheric conditions. These flow conditions result in Reynolds numbers over 2.7 million at the test section inlet. Further details on the design of the CTF can be found in the thesis work of Allison (2).

Test Section

The cascade test section is shown in Figure 3.2.

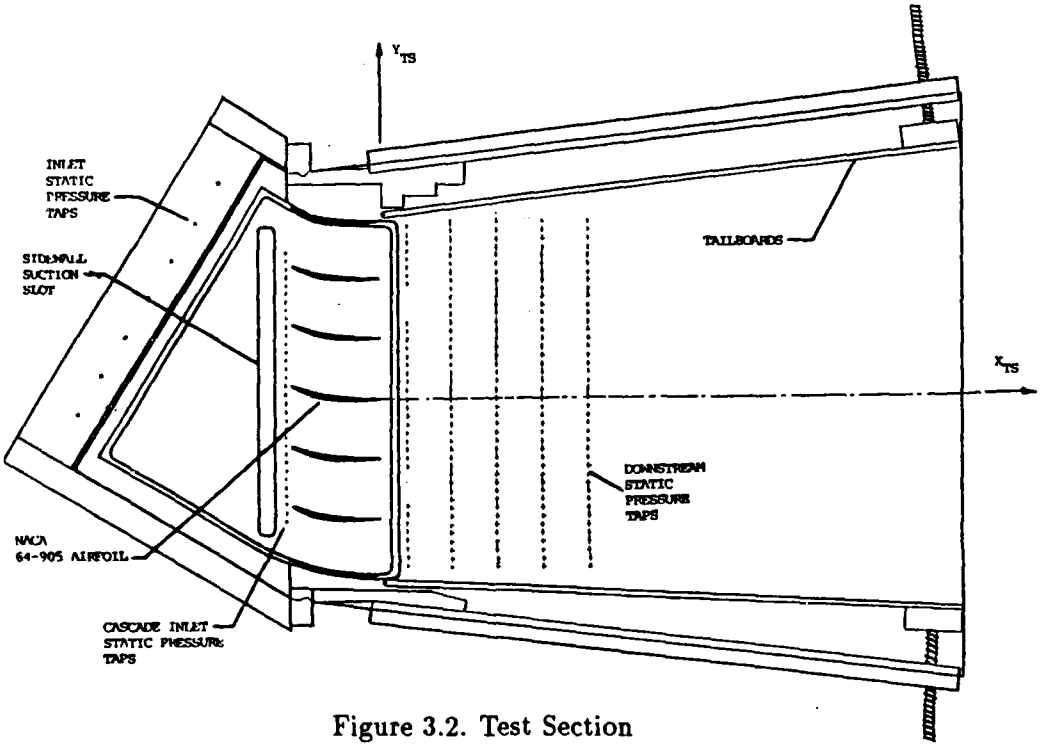

Figure 3.2. Test Section

The test section consists of a metal framework built around a seven blade cascade. The adjustable metal tailboards are the primary means of balancing the test section (i.e., at-

taining uniform flow through the cascade). The sidewalls are made of three-quarter inch plexiglass. Static pressure taps are located at strategic locations throughout the test section. There are seven taps located across the inlet throat, 33 taps immediately upstream of the cascade, and five rows of 43 taps spaced at one inch intervals downstream of the cascade. These pressure taps aid in determining the flow conditions at various points in the test section.

The cascade itself consists of seven NACA 64-905 airfoils made of molded high temperature epoxy resin. This airfoil approximates the shape of a typical compressor outlet guide vane. The outermost airfoils form an extension of the test section channel walls. The two-inch chord blades form an 8-inch by 2-inch cascade section with 1.333 inch pitch spacing. The specific blade geometry of a single blade is shown in Figure 3.3, while Figure 3.4 reflects a three blade portion of the cascade. The pertinent blade/cascade geometry is summarized in Appendix B.

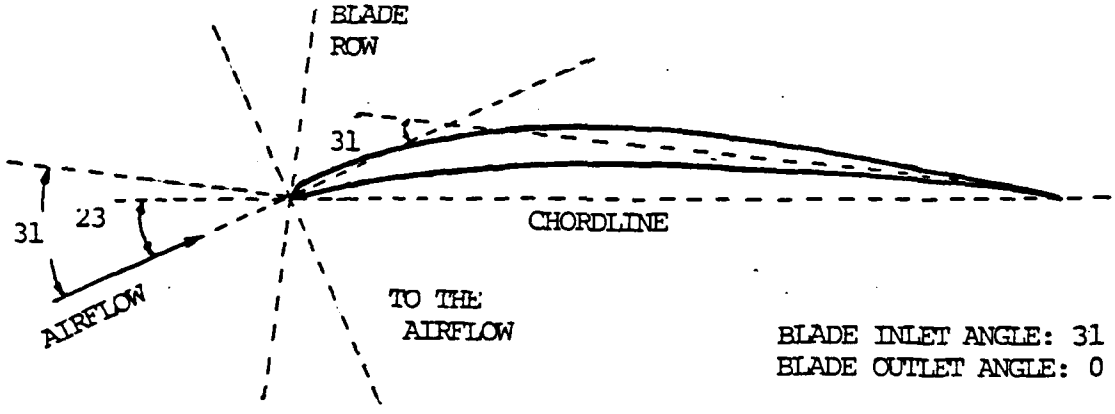

Figure 3.3. NACA 65-905 Blade

This investigation examines the downstream flowfield characteristics of three different blade configurations. These blade configurations are illustrated in Figure 3.5. Configuration #1 is the uncrenulated blade and serves as the baseline blade. The effects of a small

number of large crenulations are studied using Configuration #2, and Configuration #3 reflects a greater number of smaller crenulations.

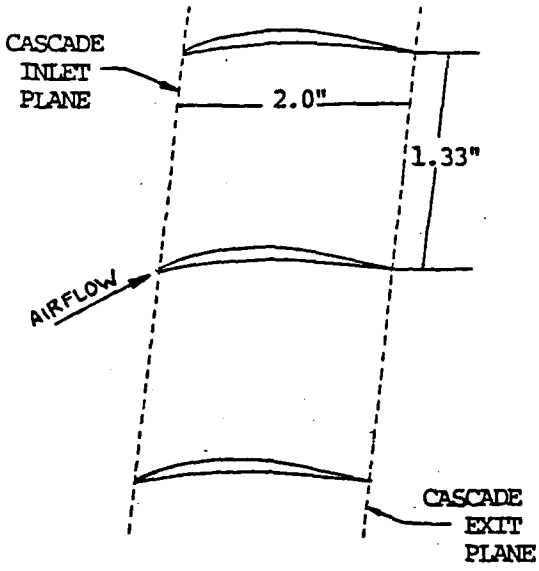

Figure 3.4. Three Blade Cascade Portion

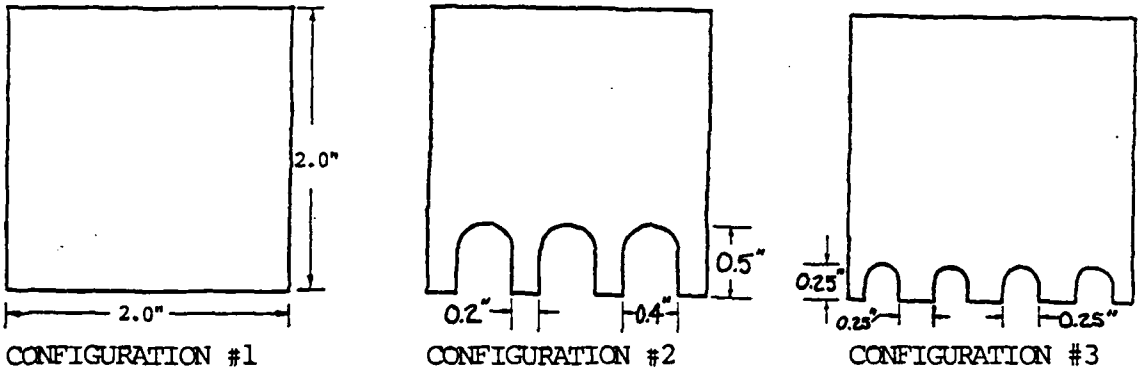

Figure 3.5. Blade Configurations

To achieve meaningful results, some form of boundary layer control is required to ensure two-dimensional flow in the cascade (9:31). The boundary layer control mechanisms used in this test section are adjustable sidewall slots (shown in Figure 3.2) located 0.4

inches upstream of the cascade blade row. An industrial vacuum cleaner provides the suction needed to draw off the boundary layer through these slots.

To gain an understanding of the flow in the cascade blade channel, a blade with static pressure taps on the pressure surface and a blade with static pressure taps on the suction surface are used to measure the blade pressure distributions. Figure 3.6 illustrates these pressure tapped blades. Pressure tap locations are summarized in Appendix B.

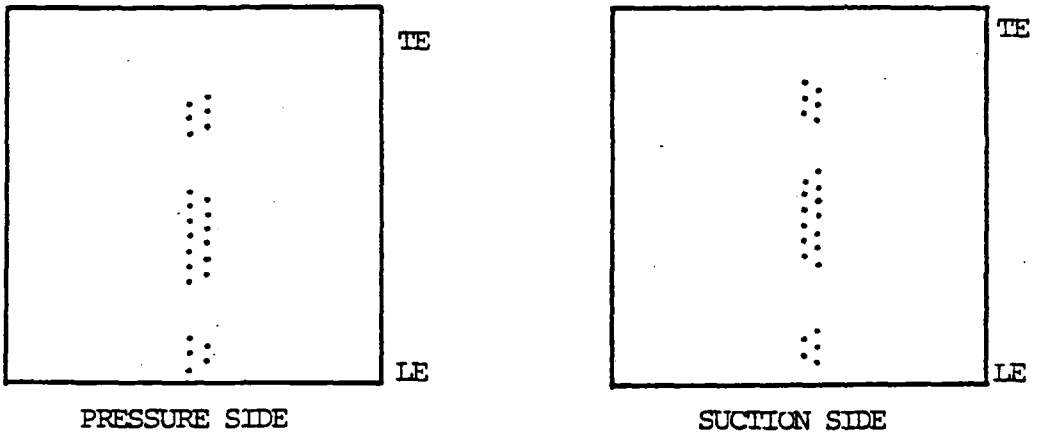

Figure 3.6. Tapped Blade

Instrumentation

Velocity and turbulence data are collected using a TSI 1241-10 X-wire probe. A typical X-wire probe is shown in Figure 3.7.

Voltage and velocity data are used to develop a calibration law of the form

$$N_u \left(\frac{T_m}{T_f}\right)^b = A + BRe^{0.5} + CRe \qquad 3-1$$

Details on the development of the calibration law are provided in Appendix D.

The X-wire probe was selected for this investigation because it indicates flow direction as well as flow velocity. By aligning the probe with the axial X-direction of the test section, axial velocities and exit flow angles can be measured directly. Some trigonometric

manipulations and a knowledge of probe geometry are required to determine the X and Y velocity components. Details on these relationships are discussed in Appendix E.

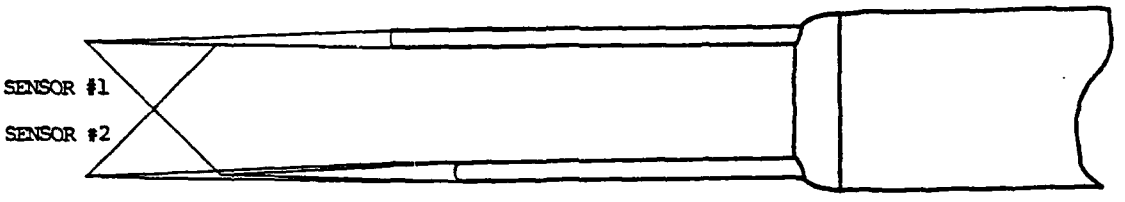

Figure 3.7. X-wire Probe

Turbulence levels in the flow can also be measured with the X-wire. The equation for the relative turbulence level, σ, cited by Cebeci (4:13) is used in this study and is discussed in greater detail in Appendix F.

$$\sigma = \frac{1}{|V|}\sqrt{\frac{\bar{u}^2 + \bar{v}^2}{2}} \qquad 3-2$$

A special total pressure rake designed by the author and shown in Figure 3.8 was used to conduct total pressure surveys of the cascade's downstream flow field. Its eleven 0.028 inch diameter tubes span 75% of the test section width, providing extensive coverage of the blades' spanwise total pressure distributions.

The traversing mechanism shown in Figure 3.9 positions either the X-wire probe or the total pressure rake in the flow field. An airfoil shaped fairing reduces the aerodynamic interference of the probe mount and lessens probe support vibration. Movement in the X and Y directions is computer controlled while position in the Z direction must be set manually. Digital encoders display the X position with 0.002 inch resolution and the Y position with 0.001 inch resolution.

The Hewlett Packard 3052A Data Acquisition System handles the data acquisition and computational reduction for the AFIT Cascade Test Facility. A Hewlett Packard 9845B computer controls the various peripherals including two eight-inch disk drives, a printer, a plotter, a voltmeter, a scanivalve system, a channel scanner, and the traversing mechanism. Appendix A contains a listing of system components and model numbers. The data acquisition system uses 4 copper-constantan thermocouples to monitor the stilling chamber total temperature, the ambient temperature, and the X-wire calibrator temperatures. Pressure transducers monitor the stilling tank total pressure, the ambient pressure, the X-wire calibrator pressures, and the test section inlet and exit pressures. Calibration of the pressure transducers is discussed in Appendix C. Data acquisition programs are typically used to automate the data collection process. The computer stores the raw data on eight-inch floppy disks. This data is later reduced into usable engineering units by data reduction programs written expressly for this computer system.

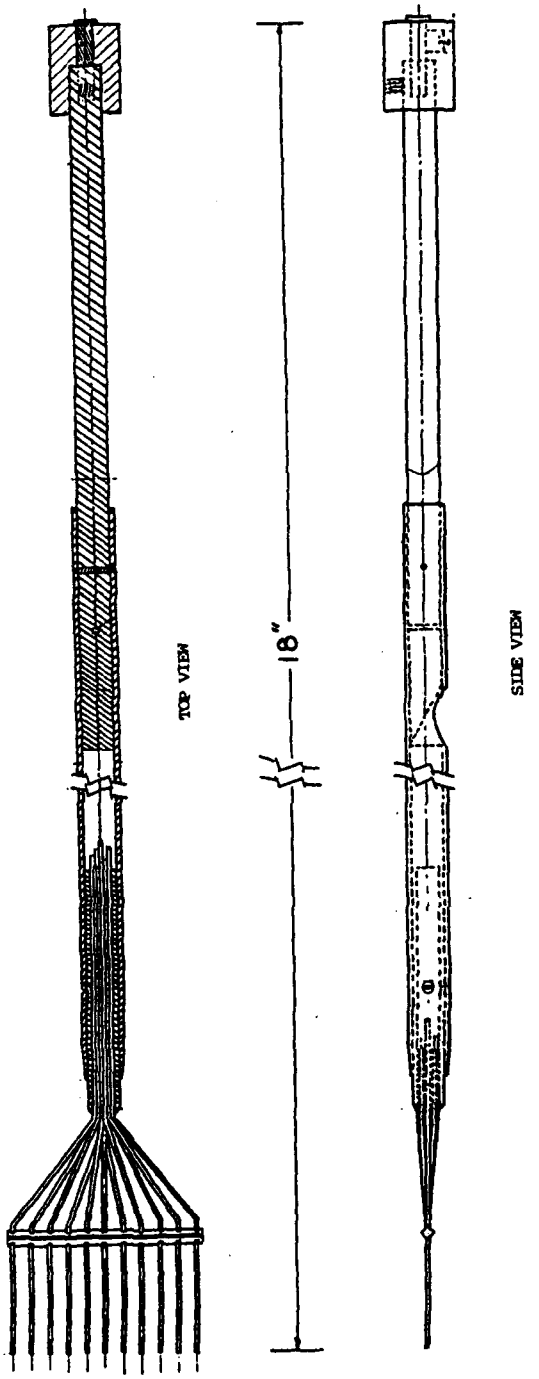

Figure 3.8. Pressure Rake

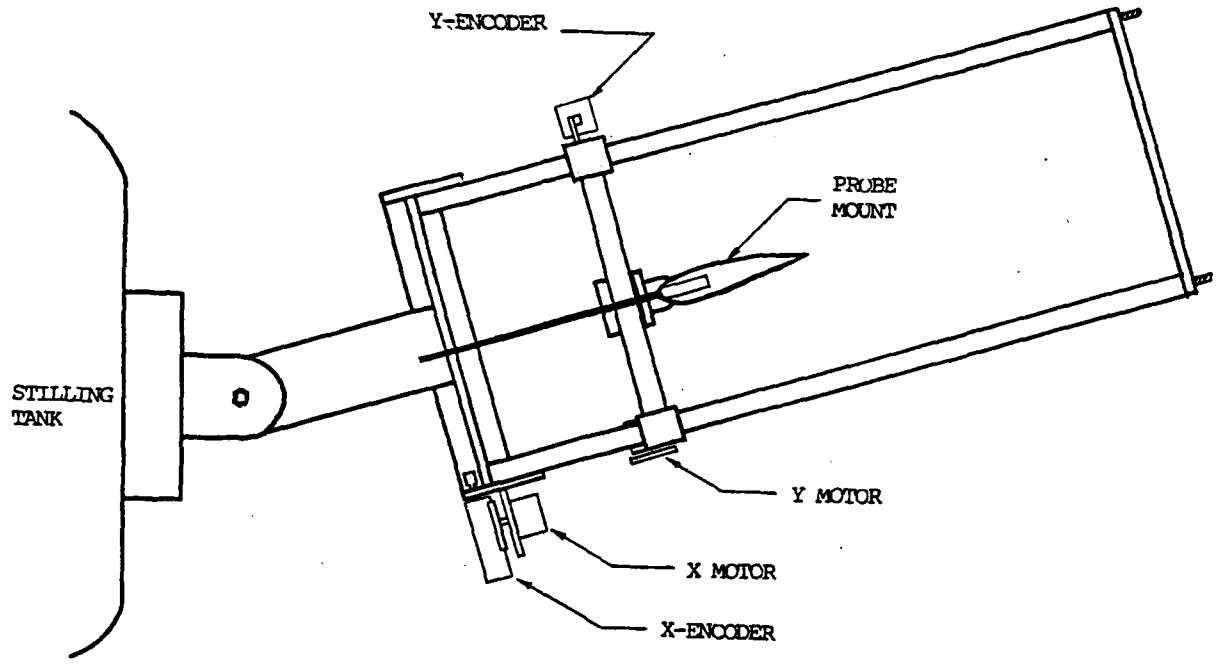

Figure 3.9. Traversing Mechanism

IV. Results and Discussion

Balancing the Test Section for Flow Periodicity

The first task in the investigation was establishing uniform flow through the cascade with the baseline uncrenulated blades installed. The 33 static pressure taps upstream of the cascade were monitored with the scanivalve, and the tailboards were adjusted until the pressure profile of the flow entering the cascade was periodic across the three inner blade spacings. Figure 4.1 shows this periodic pressure profile. The flow through the test section is subsonic and it exhausts to the atmosphere. These flow conditions cause sub-atmospheric pressures to occur at the cascade inlet. The static inlet pressure and the stilling tank total pressure are measured in psig, so non-dimensionalized pressure is negative.

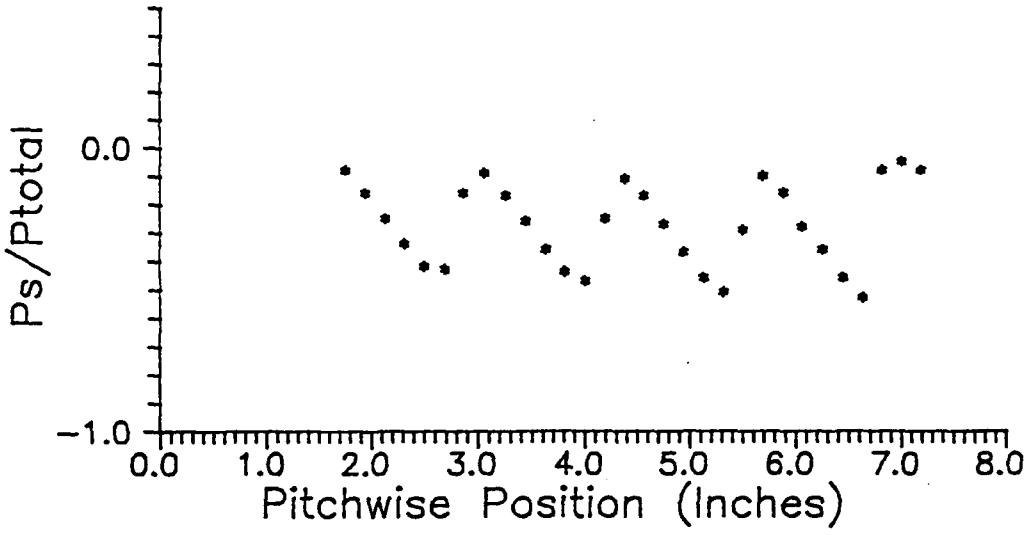

Figure 4.1. Static Pressures Across Three Blade Spacings

After positioning the tailboards, a pitchwise traverse with an X-wire probe was made 1.6 inches downstream of the cascade exit plane. The X-wire measures the X and Y components of the flow velocity, so the flow magnitude and direction can be plotted as shown in Figure 4.2 which shows the results of a center span traverse. When the test section is properly balanced, the freestream velocity remains constant over the pitch length

of the cascade. The test section tailboards were adjusted until the freestream velocity in an exit plane spanning the middle three blades did not vary by more than one percent.

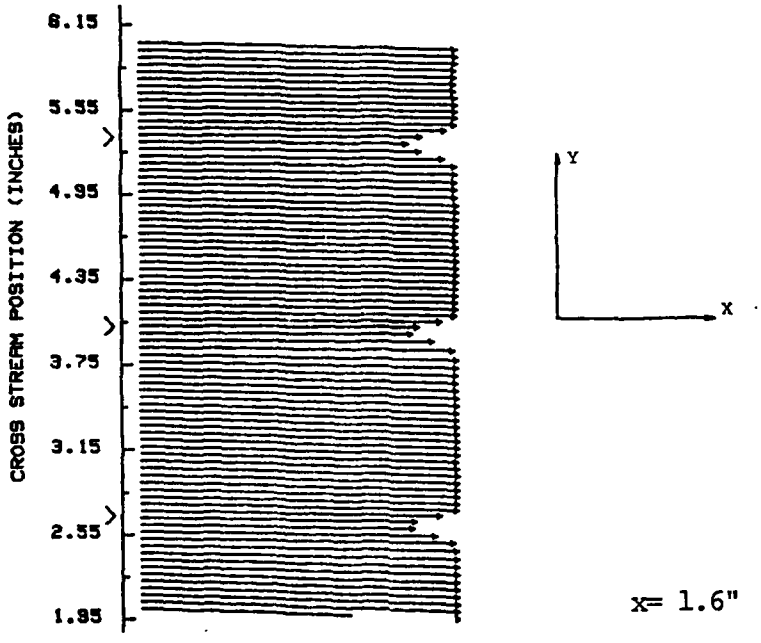

Figure 4.2. Pitchwise Velocity Traverse

Once determined, the tailboard positions remained fixed for all blade configurations. This was done to avoid introducing flowfield differences due to changes in the test section geometry. The tailboard geometry established a constant area exit plane of 16.05 square inches ($2'' \times 8.025''$).

Test Section Flow Quality

Several assumptions are made about the flow in a two-dimensional cascade, the most important being that the flow is two-dimensional, at least in the region of data collection. The primary method used in this investigation to determine the region of two-dimensional flow across the blade span was oil drop flow visualization. Matrices of 64 oil drops, such as shown in Figure 4.3, were applied to the pressure and suction surfaces of the three inner blades of the cascade. The flow was started for approximately five to ten seconds.

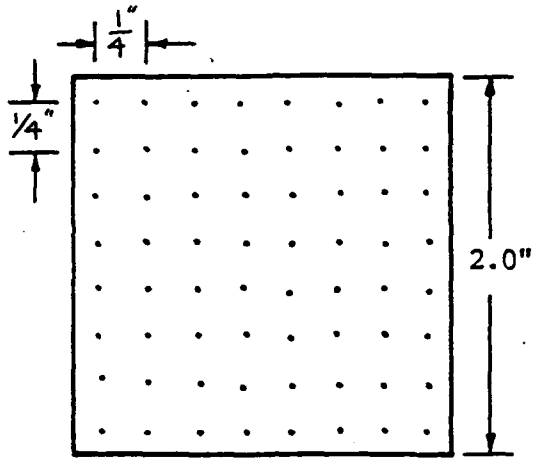

Figure 4.3. Oil Drop Pattern

The effect of the sidewall suction on the nature of the flow can be clearly seen by comparing Figure 4.4 (no suction applied) to Figure 4.5 (suction applied). The streamlines on the blade with no boundary layer suction are forced toward the middle of the span by the large corner vortex initiated by the sidewall boundary layer. When sidewall suction is applied, this boundary layer is drawn off immediately upstream of the cascade. This reduces the thickness of the sidewall boundary layer along the blade length and the flow across the span remains more uniform. Without any boundary layer control, the region of two-dimensional flow on the suction surface of the blade is limited to roughly 25% of the blade span. With sidewall suction applied, this region is extended to approximately the middle 50% of the blade span. The flow patterns on other blades, to either side of the center blade, are included in Appendix G. The flow patterns are very similar over the three blade surfaces. The flow pattern on the pressure side shown in Figure 4.6 was typical for all three blades. The flow on this side does not experience the extreme adverse pressure gradient of the suction side, so its flow pattern is much more uniform. To further clarify the flow on the suction surface, the corner vortices shown in Figure 4.5 were investigated.

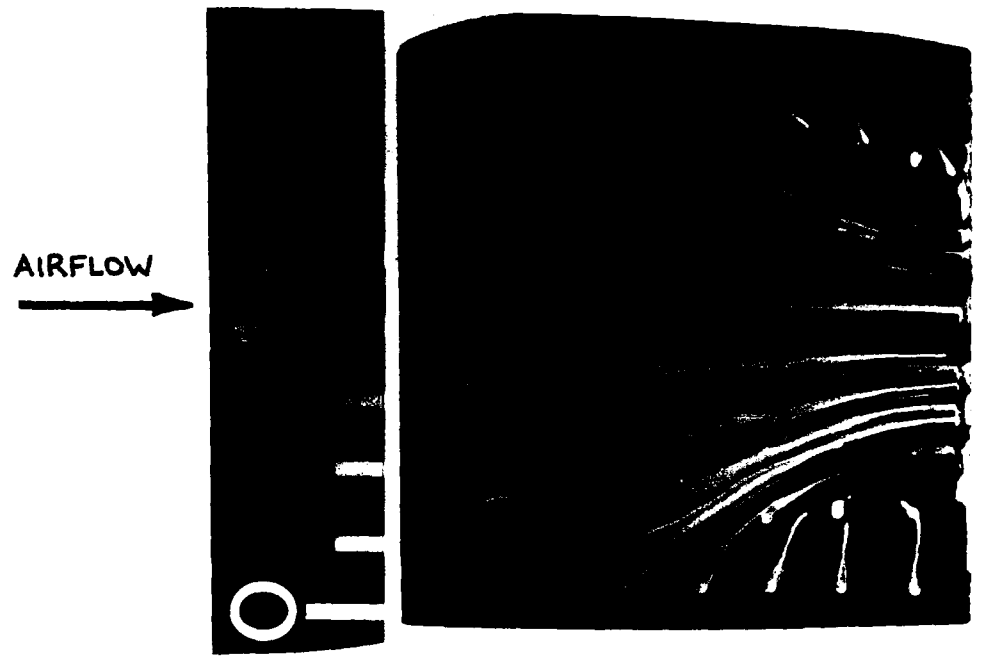

Figure 4.4. Flow Pattern - Suction Side - No Sidewall Suction

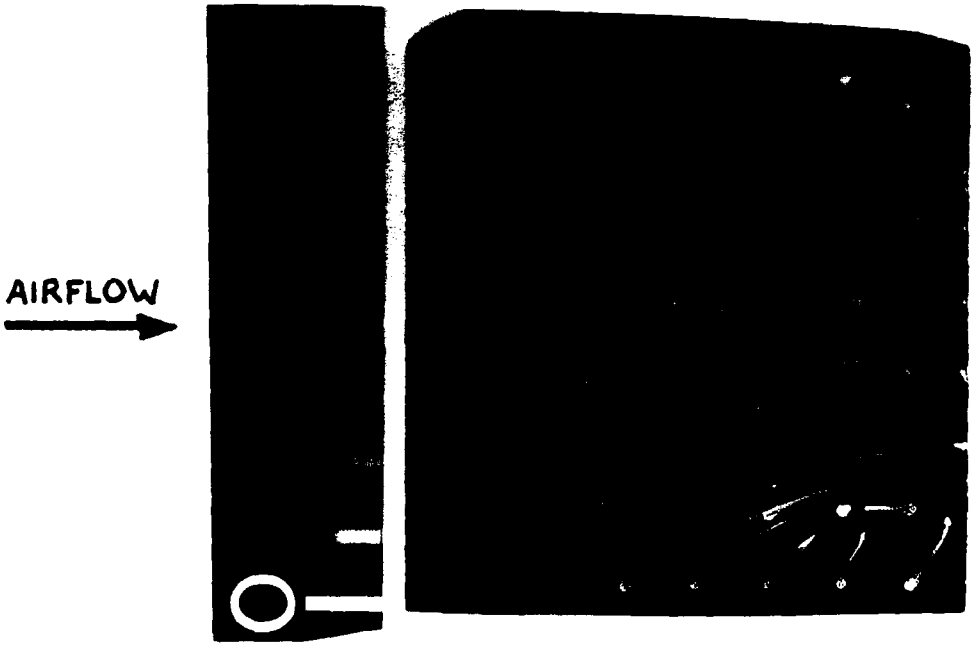

Figure 4.5. Flow Pattern - Suction Side - Sidewall Suction Applied

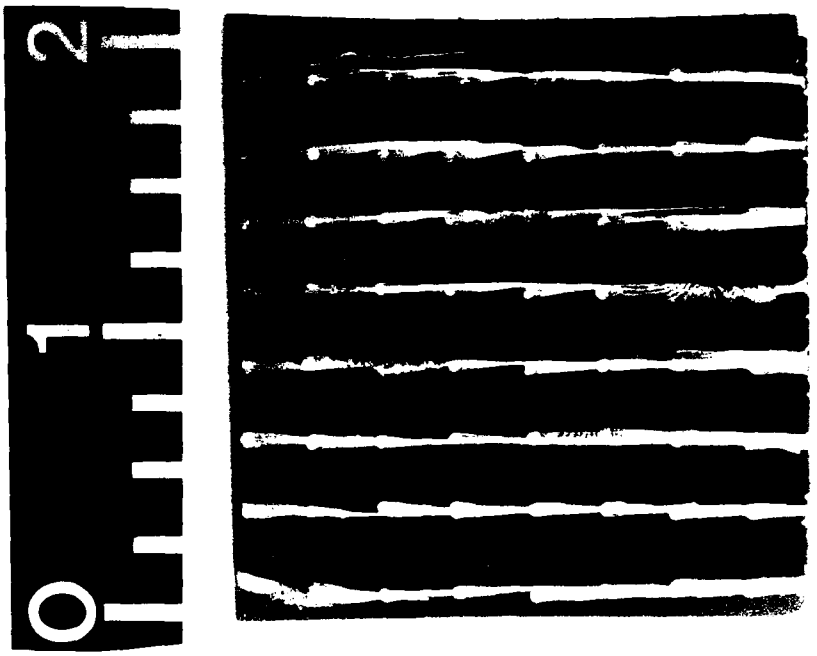

Figure 4.6. Flow Pattern - Pressure Side - Sidewall Suction Applied

In the corner vortex areas, some of the oil dots are stagnant and others actually indicate a flow reversal towards the leading edge. These flow reversals appear to be created by the flow interacting with the wall boundary layer. To investigate this phenomenon further, another oil drop matrix was applied to the suction surface of the center blade and the flow turned on for over two minutes. The general flow pattern remained the same as in the previous run, but this time the oil drop patterns for the corner vortices were allowed to fully develop. (Figure 4.7 illustrates this flow pattern.) At the center of each vortex, the oil pooled together as shown. As will be discussed later, these vortices have an effect on the flow through the cascade.

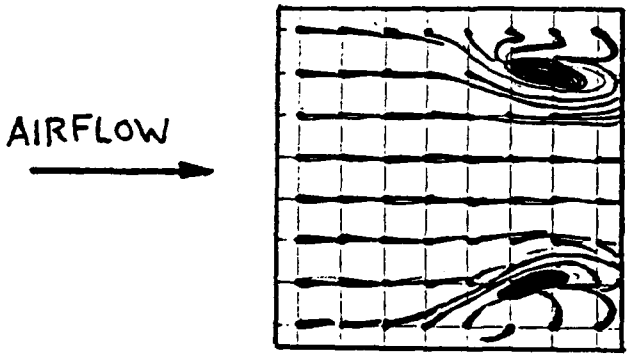

Figure 4.7. Corner Vortex Development

Another indicator of flowfield two-dimensionality is the Axial Velocity Density Ratio (AVDR). As discussed in Chapter 2, AVDR values between 0.8 and 1.2 indicate that quasi-two-dimensional flow can be assumed. The AVDR values across the middle inch of the blade span ranged from a low of 0.9525 to a high value of 1.0187 over the three blade configurations. This also indicates that two-dimensional flow was achieved.

In addition to two-dimensional flow, two other flow quality measurements were made in the test section. The first determined the static pressure distribution across the inlet to the test section, and the second measured the pitchwise static pressures downstream of the cascade. Figure 4.8 illustrates the constant pressure distribution over the seven sidewall pressure taps spanning the test section inlet. The sidewall static pressures parallel to the cascade exit plane were measured 1.6 inches downstream of the cascade, the second row of taps shown in Figure 3.2. The pressure distribution as shown in Figure 4.9 is very uniform, especially around tap #21, which is located on the test section axial centerline. Pressure taps #13-#29 span the three middle blades of the cascade. These pressure surveys verify the assumptions made about constant pressure conditions in the test section.

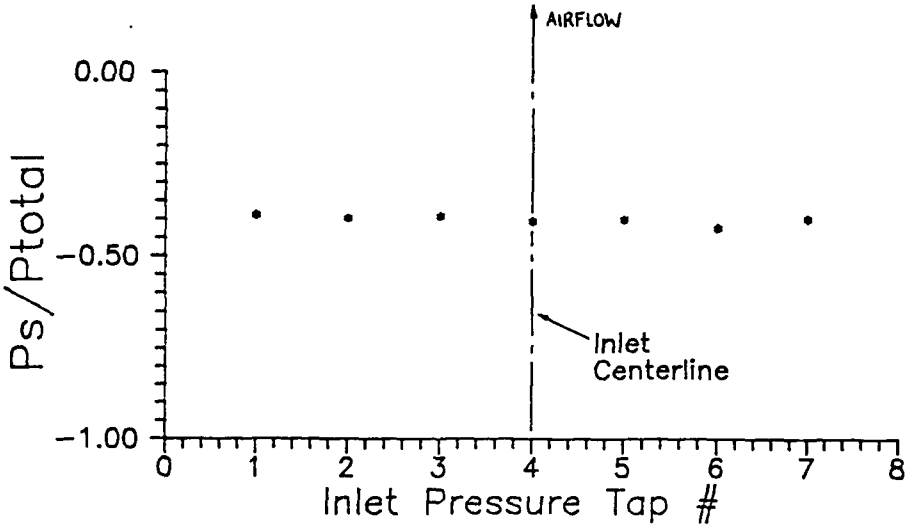

Figure 4.8. Inlet Static Pressure Profile

Blade surface pressure surveys yield further information on the nature of the flow

through the cascade. A plot of the pressure coefficient versus blade position for both blade surfaces is shown in Figure 4.10. The gradual increase in the pressure coefficient on the blade's suction surface from leading edge to trailing edge, coupled with oil drop movement at the blade's midspan, indicate that the flow does not separate on the blade. Other researchers have found that sidewall vortices, such as the corner vortices discussed earlier, tend to extend the region of attached flow (14:28).

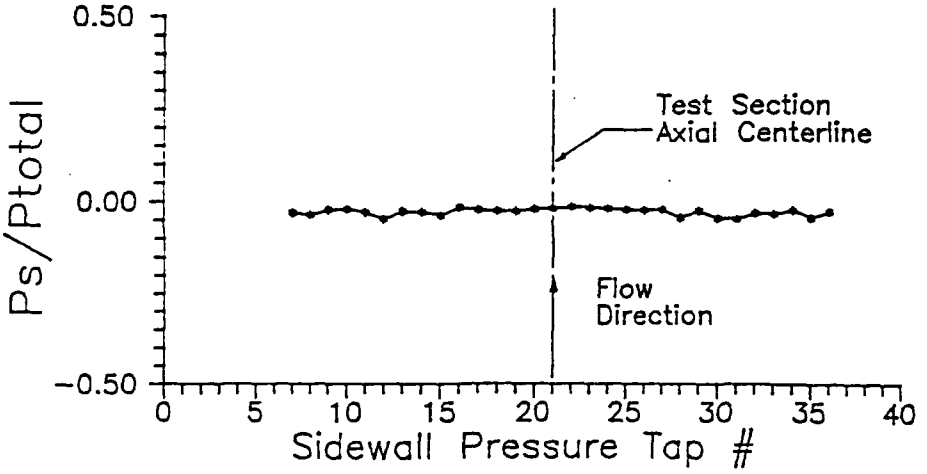

Figure 4.9. Downstream Static Sidewall Pressures

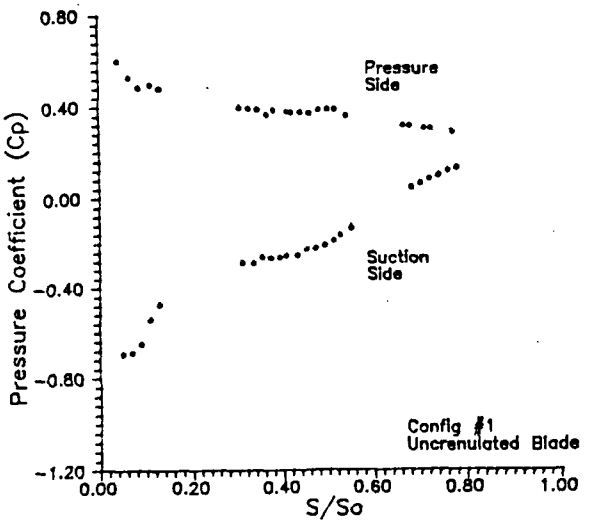

Figure 4.10. Blade Pressure Coefficient Distribution

Blade Wake Surveys

Based upon the region of two-dimensional flow in the cascade, eleven spanwise positions, centered on the trailing edge and spaced at 0.1 inch intervals as shown in Figure 4.11, were selected for data collection. This range was large enough to include the spanwise effects of the crenulations while still remaining in the region of two-dimensional flow. For each spanwise position, three pitchwise traverses were made: 0.6, 2.6, and 4.6 inches downstream of the cascade exit. These surveys were over one blade spacing and focused on the wake generated by the center blade.

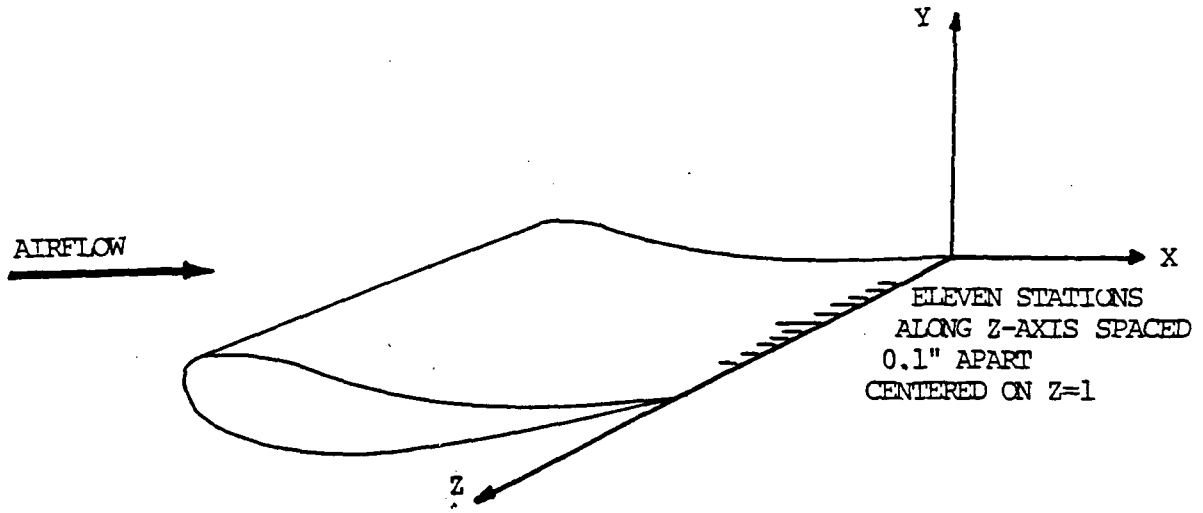

Figure 4.11. Spanwise Data Collection Points

The X-wire probe and the pressure rake were each axially aligned with the X direction of the test section as shown in Figure 4.12. The use of both an X-wire probe and a total pressure rake provided two independent methods of calculating total pressure. Figure 4.13 illustrates the close agreement between X-wire and pressure rake measurements in the second (x = 2.6 inches) and third (x = 4.6 inches) traverses of blade configuration #1, the uncrenulated blade. Similar measurement comparisons for blade configurations #2 and #3 are included in Appendix G (Figures G.3 and G.4). They also show good agreement between hot wire and pressure rake total pressure measurements. In the traverse immediately downstream of the cascade (x = 0.6 inches), complex flow conditions resulted

in questionable hot wire measurements. Consequently, only hot wire data obtained in the second and third traverses were used in evaluating the flowfields of the various blade configurations.

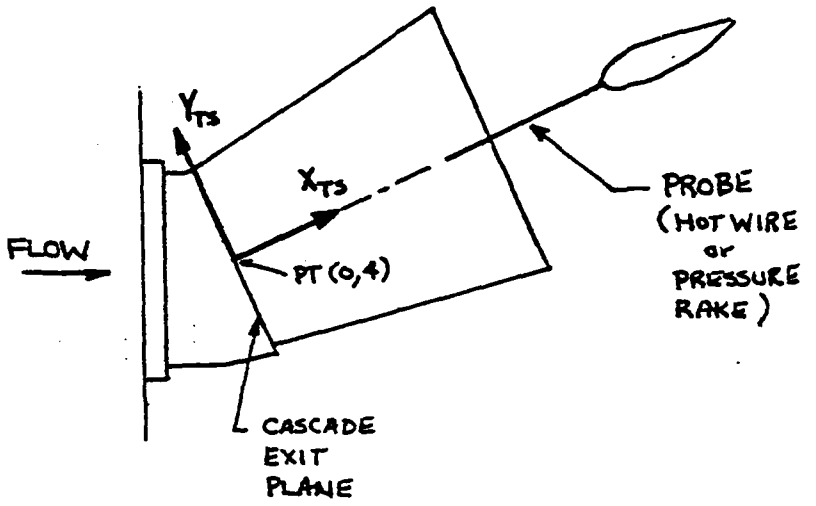

Figure 4.12. Test Section Alignment

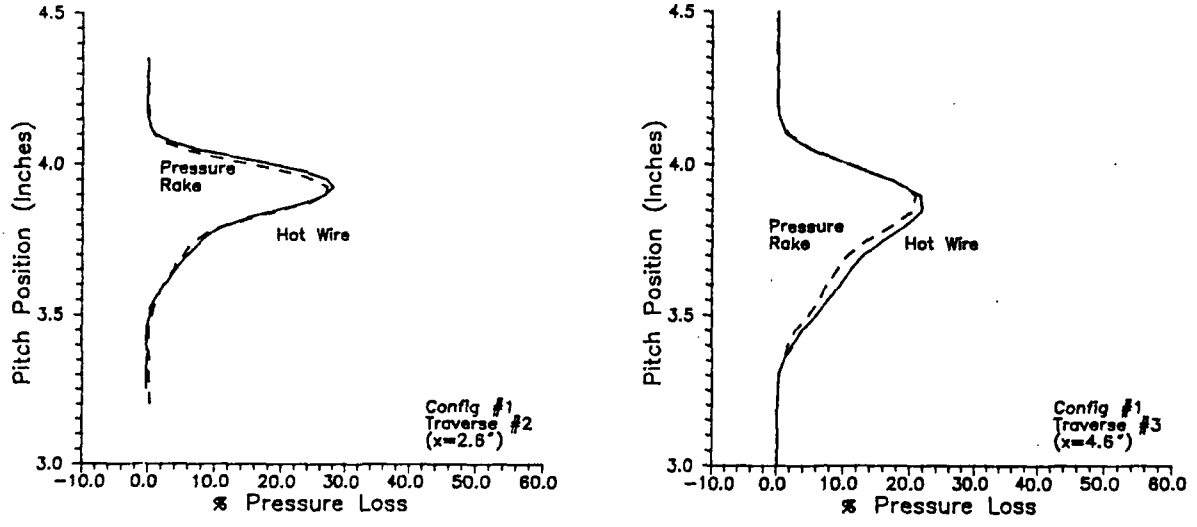

Figure 4.13. Configuration #1 - Pressure Profiles

A qualitative feel for how the crenulations alter the flowfield can be obtained by

looking at three-dimensional plots of velocity, Figures 4.14, 4.15, and 4.16, which show how the wake dissipation from x = 2.6 inches to x = 4.6 inches varies among the blade configurations. The exit velocity data was obtained using an X-wire probe and has been non-dimensionalized by dividing by the test section inlet velocity. The velocity contours of the uncrenulated configuration, shown in Figure 4.14, are very uniform across the blade midspan. As the flow proceeds from traverse #2 (x = 2.6 inches) to traverse #3 (x = 4.6 inches), the wake dissipates evenly. The slightly broader wakes at the outer fringes of the contours indicate where the flow is becoming less two-dimensional. With the large crenulations (configuration #2, see Figure 4.15), the counterrotating vortices create two regions of increased velocity in the wake which persist in the flow as it moves downstream. These regions of increased velocity aid in re-energizing the wake and reducing its velocity deficit. Figure 4.16 shows the flow pattern of configuraion #3. The smaller crenulations do not produce the strong velocity variations seen in the wake of configuration #2, but some flow perturbations are visible in the traverse at x = 2.6 inches (traverse #2). As the flow moves downstream, the effects of the crenulations diminish and by the third traverse (x = 4.6 inches) they are barely discernible. A comparison of Figures 4.15 and 4.16 indicates that larger crenulations create larger and more persistent flow variations in the wake.

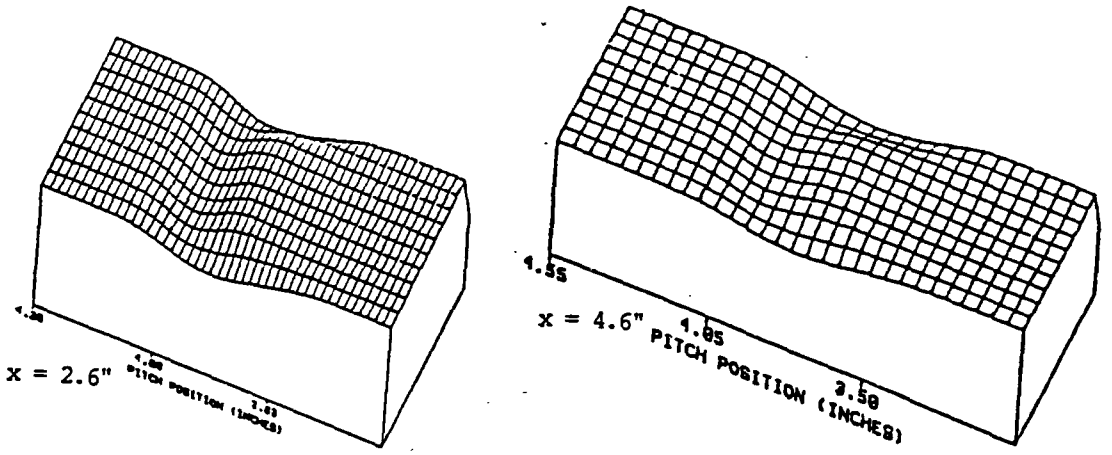

Figure 4.14. Configuration #1 - 3-D Velocity Contour

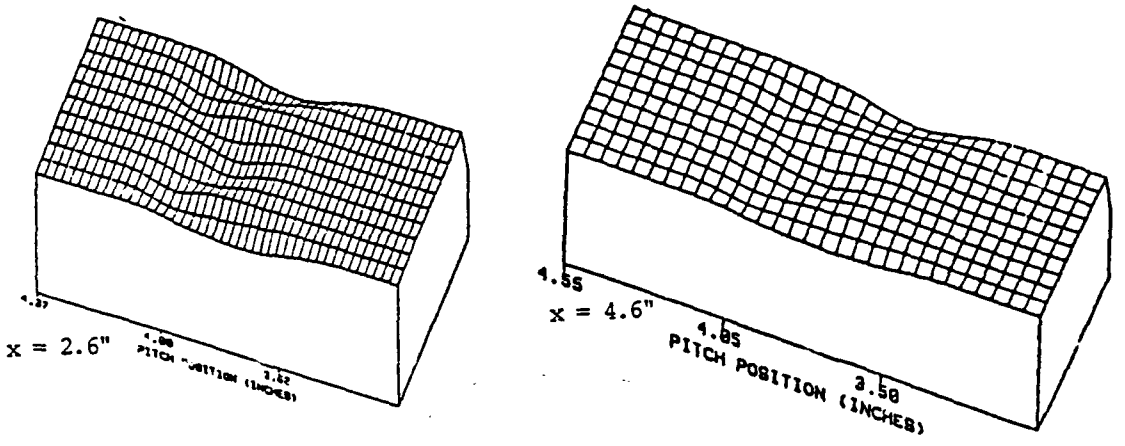

Figure 4.15. Configuration #2 - 3-D Velocity Contour

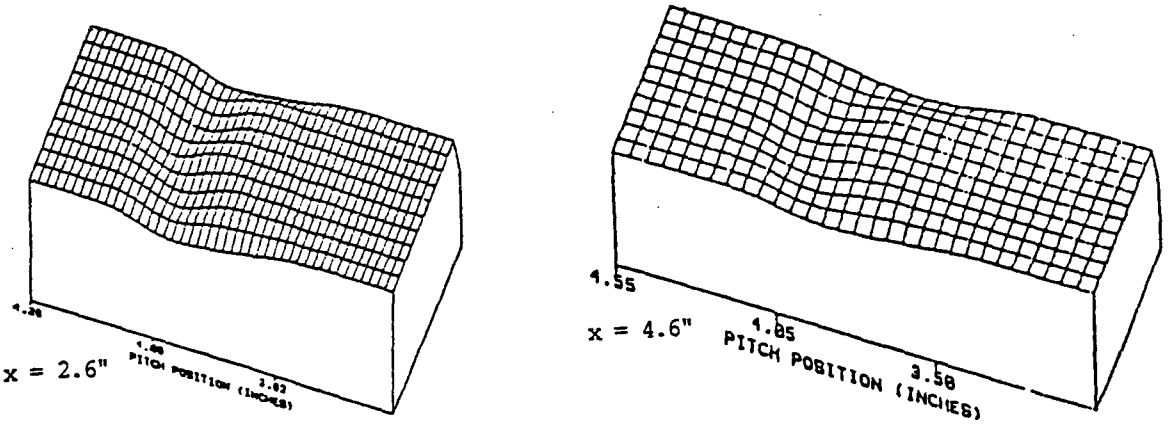

Figure 4.16. Configuration #3 - 3-D Velocity Contour

Once the velocity data was collected, a single composite velocity profile was created by averaging the data from the eleven hot wire traverses across the span of the blade. For each blade configuration, two composite velocity profiles (x = 2.6 inches and x = 4.6 inches) were generated. The composite velocity profiles, shown in Figure 4.17, illustrate some differences and similarities among the three blade configurations. Configuration #2 has a much shallower wake, which indicates a smaller wake velocity deficit.As discussed previously, this shallower wake is a result of the re-energization action of the counterrotating vortices created by the crenulations. Note the similarity between the profiles of configuration #1 and #3. This indicates that the smaller crenulations do not distort the

wake form to the same degree as the larger crenulations. However, configuration #3 does have a slightly smaller velocity deficit than the uncrenulated (configuration #1) blade's profile, indicating its crenulations also increase wake dissipation.

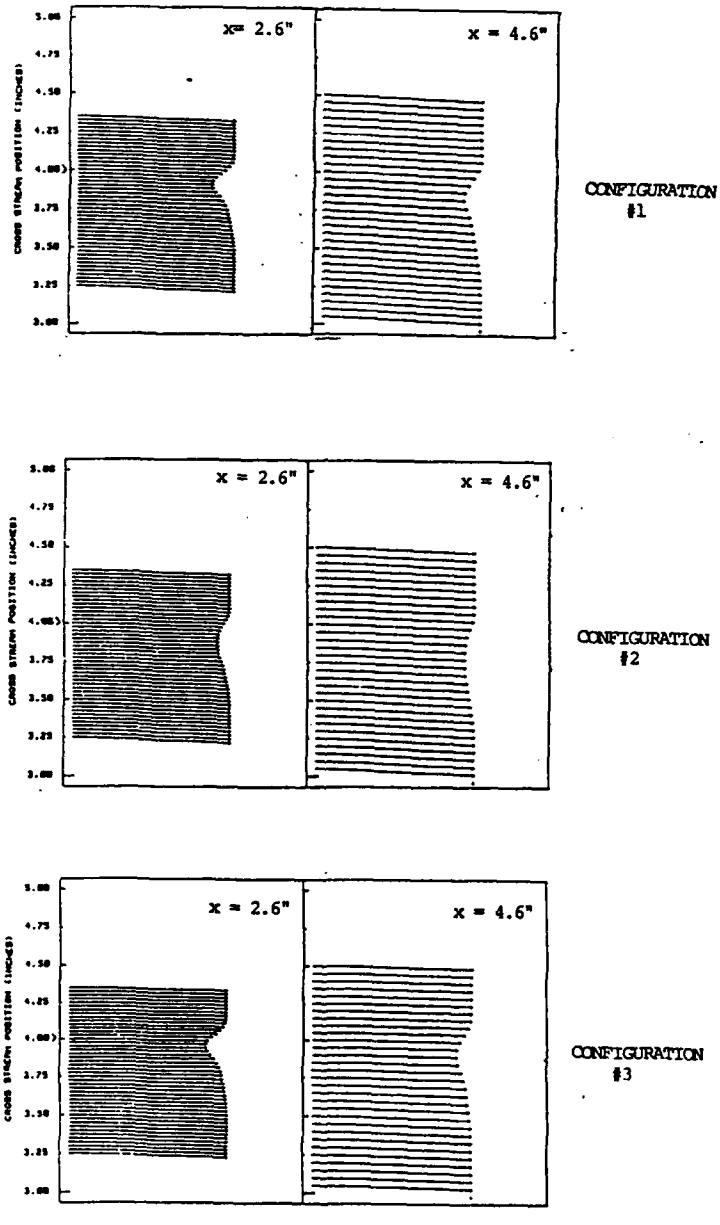

Figure 4.17. Composite Velocity Plots

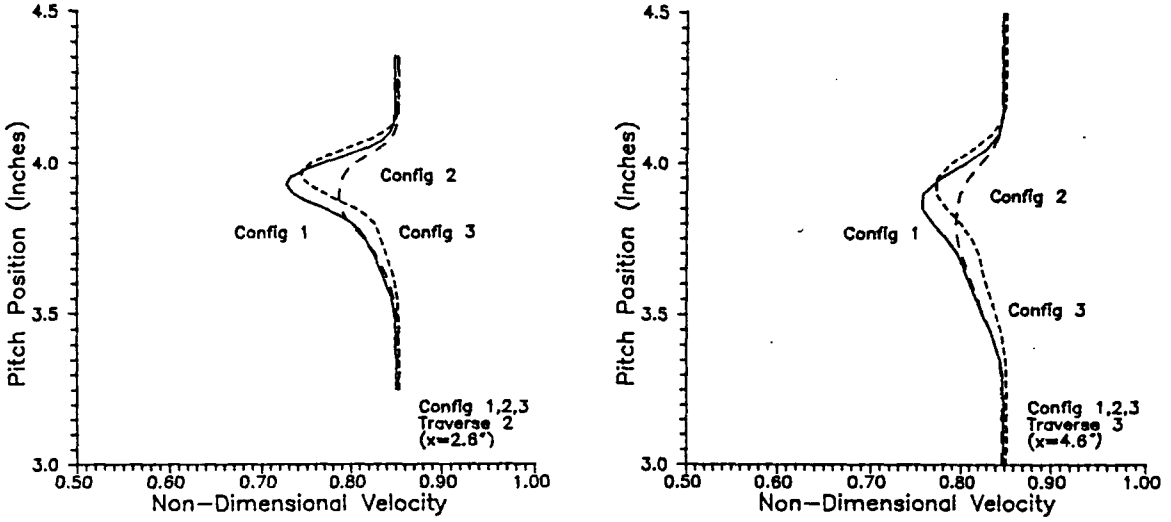

Figure 4.18. Comparison of Velocity Profiles at each Traverse

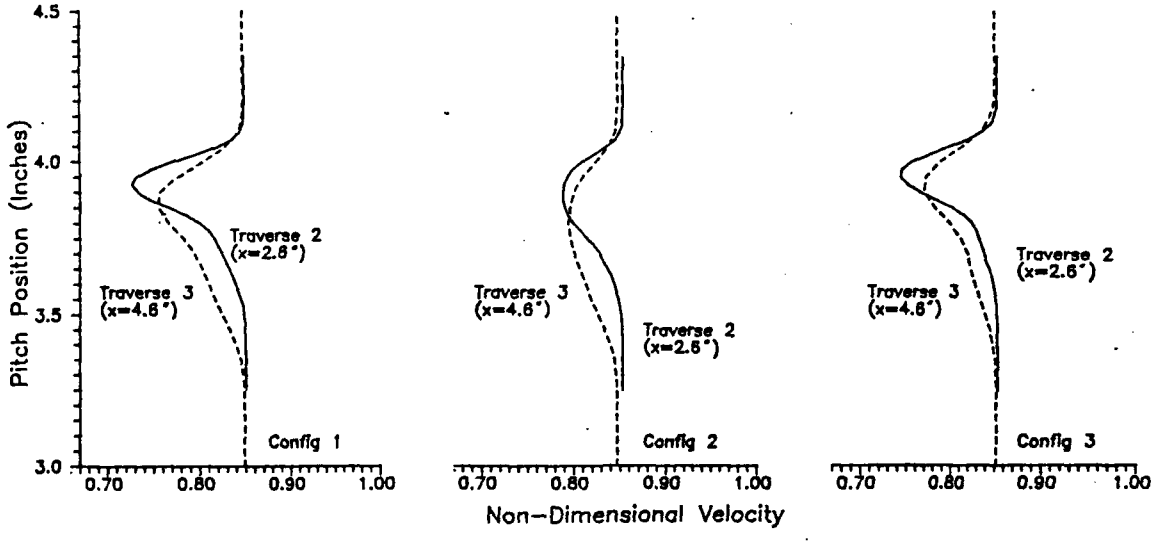

Figure 4.19. Velocity Profile Development of each Configuration

Figure 4.18 compares the composite velocity profiles of the three configurations at the two traverses and the wake dissipation patterns of the configurations are shown in Figure 4.19. All three wakes broaden and dissipate as the flow moves downstream, but configuration #1 maintains the largest wake velocity deficit. This means that the wakes of the crenulated blades dissipate and regain freestream velocity more rapidly than the wake

of the uncrenulated blade. This increased wake dissipation is a logical result of introducing counterrotating vortices into the flowfield, since these vortices increase fluid mixing.

To quantify the rate of wake dissipation, the percent wake velocity defect was calculated for each composite velocity profile. Wake velocity defect is defined to be the difference between the freestream fluid velocity external to the wake and the mass-averaged velocity over the blade spacing, divided by the freestream velocity. The smaller the percent velocity defect, the greater the wake dissipation in the velocity profile. Figure 4.20 shows that both crenulation patterns have lower percent velocity defects and hence greater wake dissipation than the uncrenulated blade. The larger crenulations (configuration #2) dissipate the wake most rapidly.

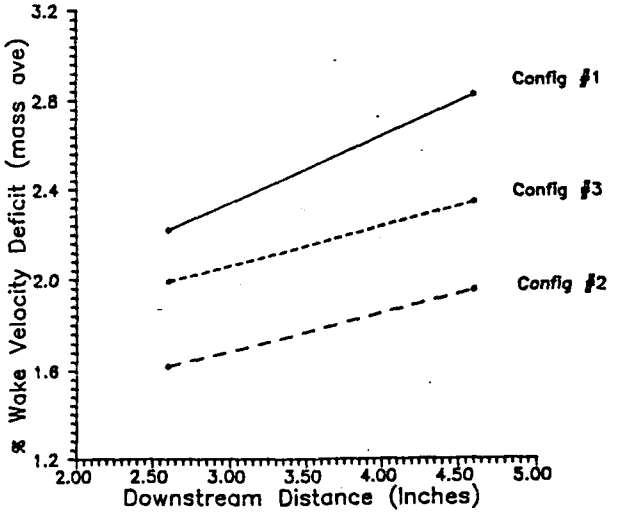

Figure 4.20. % Wake Velocity Defect

Blade Performance

Blade performance is often evaluated in terms of turning angle and total pressure loss incurred across the cascade. Figure 4.21 summarizes the measured turning angles of the three blade configurations. As can be seen, configuration #3 (small crenulations) has the greatest turning angle and configuration #1 has the smallest. An interesting point to note is that the measured turning angle of configuration #1 exceeds the theoretical turning

angle for this blade shape calculated using Carter's rule (see Appendix B for calculations) by nearly 2°. This appears to indicate that the sidewall corner vortices discussed in Chapter 3 are indeed increasing the region of attached flow and producing a turning angle greater than theoretically expected.

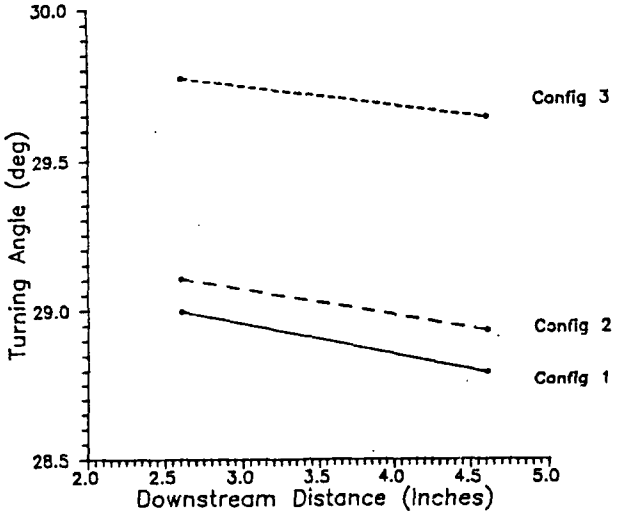

Figure 4.21. Turning Angles

With this increase in turning angle come other improvements in the flow characteristics. The level of turbulence experienced in the wake decreases with increasing turning angle as shown in Figure 4.22. Lower turbulence levels reflect lower turbulent mixing losses and result in lower total pressure losses.

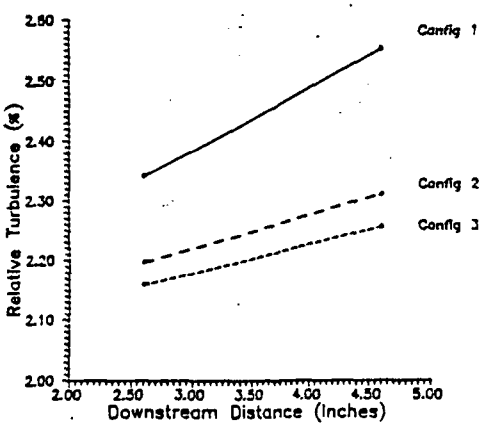

Figure 4.22. Mass-Averaged Turbulence

Only one traverse of the pressure rake was required to gather all the pressure information across the span of the blade due to the geometry of the pressure rake. A single composite total pressure profile for each traverse was created by averaging the pressures measured by the middle seven ports of the pressure rake. The pressure loss profiles resulting from these rake surveys are shown in Figure 4.23. They illustrate how the total pressure loss defects diminish as the flow moves downstream. This is due to the gradual re-energization of the wake by the freestream flow. The profiles for configuration #1 maintain the greatest pressure defect and this indicates that the uncrenulated blade has the slowest wake re-energization.

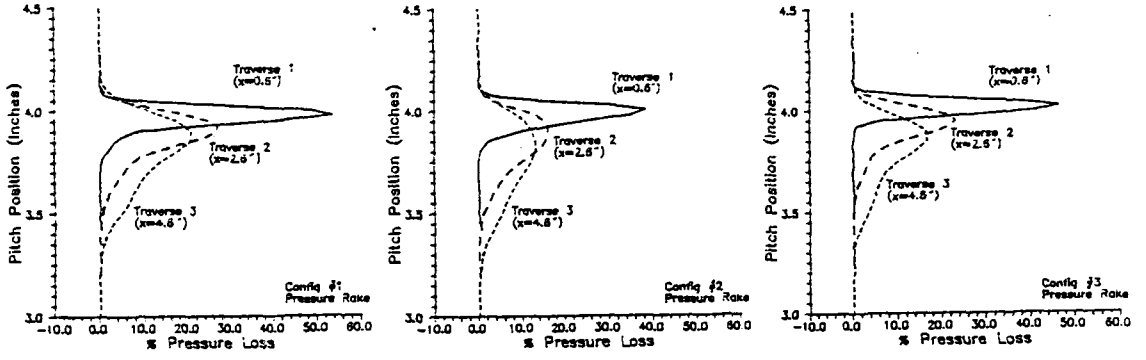

Figure 4.23. Total Pressure Loss Profiles

Percent total pressure loss across the cascade can be determined by comparing the downstream total pressure, either mass-averaged or area-averaged across one blade spacing, to the upstream total pressure across the blade spacing. Both mass-averaged (based on hot wire measurements) and area-averaged (based on pressure rake measurements) results are shown in Figure 4.24. In each case, the uncrenulated blade (configuration #1) experiences the greatest pressure losses, reflecting the poorest cascade performance.

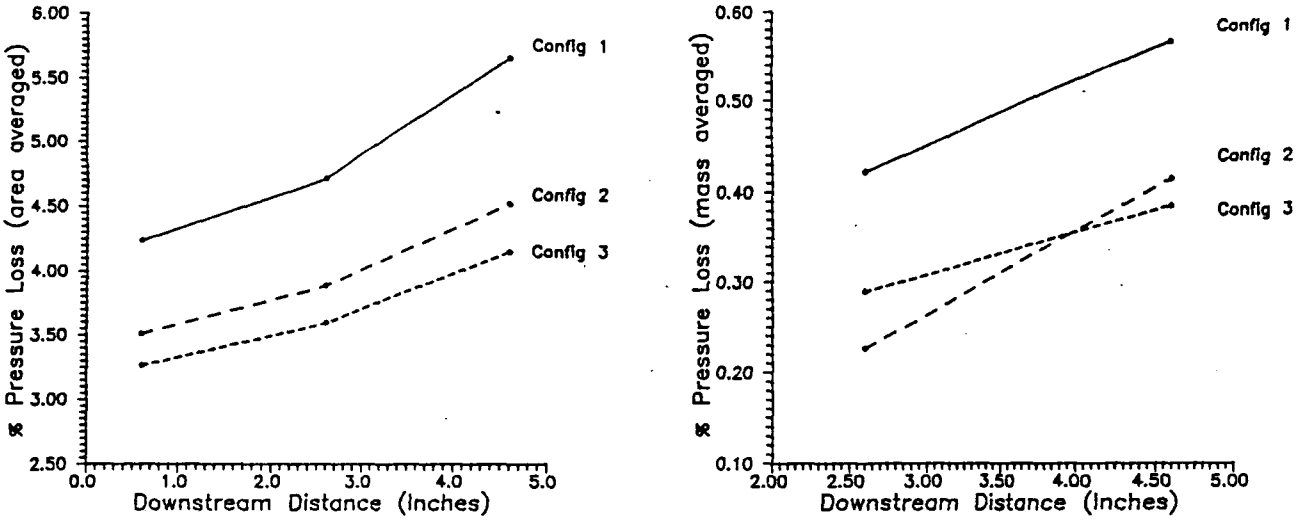

Figure 4.24. Profiles of % Pressure Loss

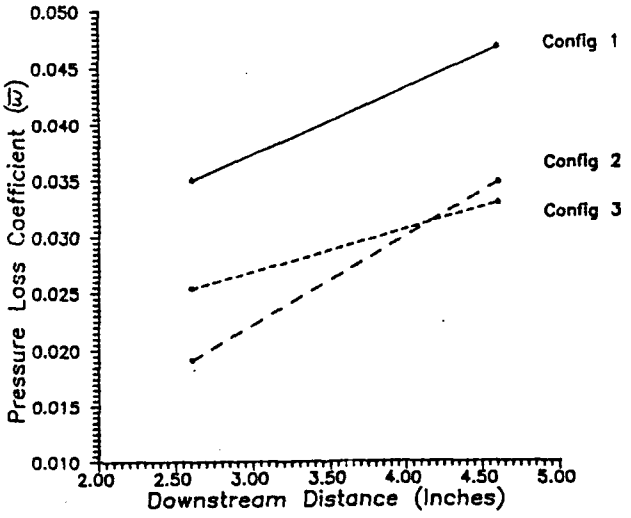

Figure 4.25. Pressure Loss Coefficient, $\overline{\omega}$)

The final flow parameter examined is the pressure loss coefficient, $\overline{\omega}$, shown in Figure 4.25. This is the typical parameter used to quantify blade performance and it is defined to be the mass-averaged total pressure loss divided by the dynamic head ($\rho V^2/2$) at the test section inlet (equation 2-2). A lower $\overline{\omega}$ indicates better performance. Configuration #1 has the highest $\overline{\omega}$ values. At x = 2.6 inches, configuration #2 has a lower $\overline{\omega}$ than configuration

#3. Moving further downstream, however, the $\overline{\omega}$ of configuration #2 increases more rapidly than that of configuration #3. At approximately 4.25 inches downstream, configuration #3 has the most favorable $\overline{\omega}$. The more rapid increase of $\overline{\omega}$ for configuration #2 could be due to the higher level of turbulence generated (see Figure 4.22) by its stronger counterrotating vortices.

Some conclusions can be drawn from the results of this investigation. Crenulations do create perturbations in the downstream flowfield which increase wake dissipation. Measurements indicate that larger crenulations generated more rapid wake dissipation, but with slighlty greater total pressure losses as fully mixed-out (i.e., wakes fully dissipated) flow is approached. This increase in wake dissipation results in less distance required for wake dissipation which could be translated into length and weight savings in a gas turbine engine diffuser. The smaller crenulation pattern had the best performance in terms of both turning angle and pressure loss coefficient. This implies that some optimization of crenulation geometry may exist which capitalizes on the wake dissipation qualitites of large crenulations and the more favorable performance of the smaller crenulations.

The effects of the crenulation vortex - corner vortex interaction and crenulation geometry warrant further investigation. Based on the similarity between the velocity (see Figure 4.18) and pressure (see Figure 4.23) profiles of the uncrenulated baseline blade and those of configuration #3, it is hypothesized that the improved flow characteristics of configuration #3 are due mainly to the increased flow turning angle possibly induced by the crenulation vortex - corner vortex interaction. Configuration #2 (large crenulations), however, demonstrates sustained wake deformations resulting from the crenulations' counterrotating vortices. In all areas considered (wake dissipation, turning angle, and total pressure loss), the crenulated blades outperformed the baseline, uncrenulated configuration.

Summary

The wake characteristics of three blade configurations, a baseline uncrenulated blade and two different crenulated blade patterns (one large and one small), were investigated in a two-dimensional cascade. The velocity and total pressure distributions across the middle blade spacing were determined using hot wire anemometry and a total pressure rake. Data was collected across the middle one inch of the blade's span at 0.6 inches, 2.6 inches, and 4.6 inches downstream from the cascade exit plane. Three-dimensional velocity contours generated from the hot wire measurements provided a qualitative picture of the crenulations' effects on the flowfield. Composite velocity and total pressure profiles were created by averaging the data taken at each x position across the blade span. These composite profiles were used to calculate the wake dissipation characteristics and the performance of each blade configuration. Percent wake velocity defect, a comparison of the mass-averaged velocity across one blade spacing with the freestream flow velocity, was used as the measure of wake dissipation. Blade configuration #2, with the larger crenulations, dissipated the wake the fastest. The blade with the smaller crenulations, configuration #3, also dissipated its wake faster than the uncrenulated baseline blade, and it also had the best performance, reflected by the greatest turning angle and the smallest pressure loss coefficient as mixed-out flow (i.e., fully dissipated wakes) was approached. Both crenulated blade configurations exhibited better wake dissipation, greater turning angles, and smaller pressure loss coefficients than the baseline uncrenulated blade.

V. Recommendations

Experimental efforts always raise additional questions deserving further investigation. Potential follow-on efforts to this thesis project are listed below in order of importance.

Boundary Layer Investigation

The results of the current thesis effort indicate that crenulations may influence the blade pressure distribution and cause an increase in flow turning angle. This increase in turning angle indicates that crenulations impact blade performance as well as wake dissipation. Boundary layer surveys with a boundary layer probe and incorporation of static pressure taps in crenulated blades would aid in understanding the effects of crenulations on blade boundary layer development.

Separation of Crenulation Vortex Effects from Corner Vortex Effects

Crenulation vortices and corner vortices both affect the flow through the cascade. It would be useful to determine how each individual set of vortices influences cascade flow characteristics. This could be done by devising a method (perhaps increased sidewall suction) to remove the corner vortices and evaluating the cascade performance with only crenulation vortices present.

Crenulation Geometry

The size and spacing of the crenulations determine the strength of the vortex effect experienced by the flow. The larger crenulation pattern dissipated the wake more rapidly, but the smaller crenulation pattern exhibited slightly better performance. By systematically varying crenulation geometry and studying the resulting flowfield variations, the relationship between the two could be investigated.

Blade Camber

The effect of crenulations on blades of differing cambers warrants further exploration. Only NACA 64-905 blades have been used in trailing edge crenulation investigations.

References

1. Abbott, Ira H., and Albert E. von Doenhoff. *Theory of Wing Sections.* New York: Dover Publications, Inc., 1959.
2. Allison, Dennis M. *Design and Evaluation of a Cascade Test Facility.* MS Thesis GAE/AA/81D-2. School of Engineering, Air Force Institute of Technology (AU), Wright-Patterson AFB OH, June 1982.
3. Bradshaw, P. *An Introduction to Turbulence and its Measurement.* New York: Pergamon Press, 1971.
4. Cebeci, Tuncer, and A. M. O. Smith. *Analysis of Turbulent Boundary Layers.* Florida: Academic Press, Inc, 1974.
5. Cohen, H., G. F. C. Rogers, and H. I. H. Saravanamuttoo. *Gas Turbine Theory* (Third Edition). New York: John Wiley & Sons, 1987.
6. Collis, D. C., and M. J. Williams. "Two-Dimensional Convection from Heated Wires at Low Reynolds Numbers," *Journal of Fluid Mechanics*, Vol 6, pp. 357-384, 1959.
7. Doebelin, Ernest O. *Measurement Systems Application and Design.* New York: McGraw-Hill Book Company, Inc., 1983.
8. Erwin, John R., and James C. Emery. *Effect of Tunnel Configuration and Testing Technique on Cascade Performance.* NACA TN-2028. Washington: National Advisory Committee for Aeronautics, 1950.
9. Gostelow, J. P. *Cascade Aerodynamics.* New York: Pergamon Press, 1984.
10. Hernandez, Enrique G. *An Interactive Computational Aerodynamics Analysis Program.* MS Thesis GAE/AA/80D-9. School of Engineering. Air Force Institute of Technology (AU), Wright-Patterson AFB OH, 1980.
11. Kreith, Frank, and William Black. *Basic Heat Transfer.* New York: Harper & Row, Publishers, 1980.
12. Lieblein, Seymour, and William H. Roudebush. *Low-Speed Wake Characteristics of Two-Dimensional Cascade and Isolated Airfoil Sections.* NACA TN-3771. Washington: National Advisory Committee for Aeronautics, 1956.
13. Lieblein, Seymour, and William H. Roudebush. *Theoretical Loss Relations for Low-Speed Two-Dimensional Cascade Flow.* NACA TN-3662. Washington: National Advisory Committee for Aeronautics, 1956.
14. Martens, N. W. *Effects of Riblets Upon Flow Separation in a Subsonic Diffuser.* MS Thesis GAE/AA/88D-23. School of Engineering. Air Force Institute of Technology (AU), Wright-Patterson AFB OH, December 1988.
15. Poulin, J. R'emy. *Surface Roughness: Its Effects on the Performance of a Two-Dimensional Compressor Cascade.* MS Thesis GAE/AA/86D-13. School of Engineering. Air Force Institute of Technology (AU), Wright-Patterson AFB OH, December 1986.

16. Roudebush, William H. and Seymour Lieblein. "Viscous Flow in Two-Dimensional Cascades," *Aerodynamic Design of Axial Flow Compressors* (Revised), edited by Irving A. Johnsen and Robert O. Bulloxk. NASA SP-36. Washington: National Aeronautics and Space Administration, 1965.

17. Schlichting, Hermann. *Boundary Layer Theory* (Sixth Edition). New York: McGraw Hill, 1979.

18. Scholz, Norbert. *Aerodynamics of Cascades, AGARD-AG-220.* Neuilly sur Seine: Advisory Group for Aerospace Research and Development, 1977.

19. TSI. *General System Information for 1050 Series Anemometry.* St Paul, Minnesota, undated.

20. Wennerstrom, Arthur J. "Vane Configuration for Fluid Wake Re-energization", United States Patent Number 4,318,669, 1982.

Appendix A. *Component Listing*

Component	Type/Model #
Pressure Transducers	
Tank Total Pressure	Statham PM60TC
Test Section Inlet Static	Statham P6TC
Test Section Exit Static	Statham P6TC
Ambient Pressure	CEC 4-326
Bridge Balance	CEC type 8-108
DC Power Supply	HP 6205C
Scanivalve System	
Pressure Transducer	PDCR 23D
Scanivalve	48S9-3003
Controller	CTLR 2/S2-S6
Scanner Position Display	J102/J104
Thermocouples	
Copper-constantan (4)	Omega T-type
Ambient Temperature	
Tank Total Temperature	
Calibrator Top Total Temperature	
Calibrator Bottom Total Temperature	
Traversing Mechanism	
Motors (2)	North American Phillips Controls K82952-M
Encoder Transducers	Astrosystems MT28-1/10

Hot Wire/Film Anemometer System

Anemometers (3)	TSI Model 1050
Monitor and Power Supply	TSI Model 1051-6
Oscilloscope	B&K Model 1570A
X-configuration Hot Film	TSI Model 1241-10
X-configuration Probe Support	TSI Model 1155-18
Calibrator (modified)	TSI Model 1125
Transformer (to heat air for calibrator)	General Radio Co. Variac Type 50-B

Data Acquisition System	HP 3052A

Computer	HP 9845B
Disk Drives (2)	HP 9885M
	HP 9885S
Channel Scanner	HP 3495A
Digital Voltmeter	HP 3455A
Printer	HP 2225A
Plotter	HP 9872S

Pressure Rake	designed by author

Appendix B. *Miscellaneous Blade Information*

Type of Blade

NACA Series 641905 a=0.5

Meaning of Blade Designation

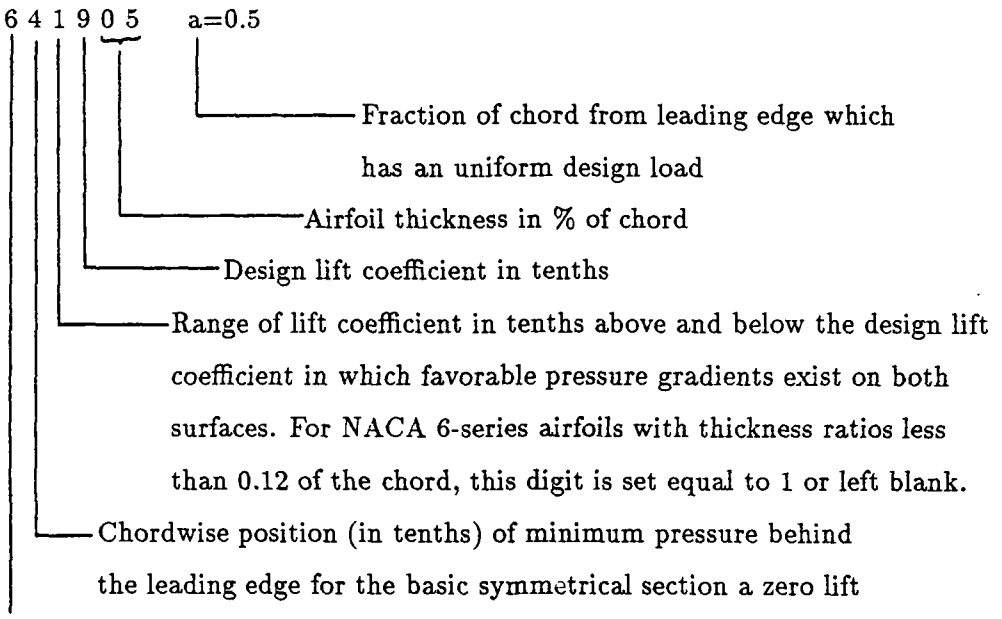

(1:120-121)

NACA a=0.5 Meanline Data

(1:399)

Table B.1. NACA a=0.5 Meanline Data

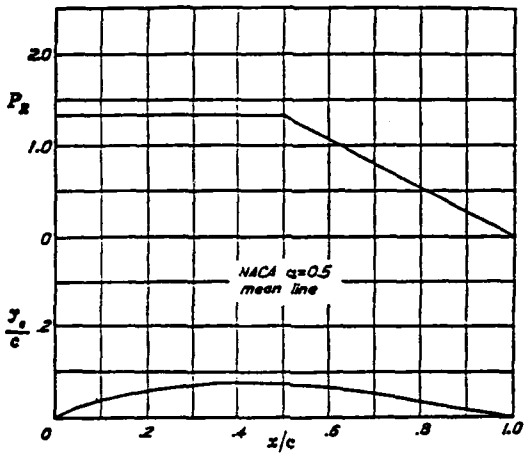

$c_{l_i} = 1.0$ $\alpha_i = 3.04°$ $c_{m_{c/4}} = -0.139$				
x (per cent c)	y_c (per cent c)	dy_c/dx	P_z	$\Delta w/V = P_z/4$
0	0			
0.5	0.345	0.58195		
0.75	0.485	0.53855		
1.25	0.735	0.48360		
2.5	1.295	0.40815		
5.0	2.205	0.33070		
7.5	2.970	0.28365		
10	3.630	0.24890		
15	4.740	0.19690	1.333	0.333
20	5.620	0.15650		
25	6.310	0.12180		
30	6.840	0.09000		
35	7.215	0.05930		
40	7.430	0.02800		
45	7.490	−0.00630		
50	7.350	−0.05305		
55	6.965	−0.09765	1.200	0.300
60	6.405	−0.12550	1.067	0.267
65	5.725	−0.14570	0.933	0.233
70	4.955	−0.16015	0.800	0.200
75	4.130	−0.16960	0.667	0.167
80	3.265	−0.17435	0.533	0.133
85	2.395	−0.17415	0.400	0.100
90	1.535	−0.16850	0.267	0.067
95	0.720	−0.15565	0.133	0.033
100	0	−0.12660	0	0

Blade Profile Coordinates

Blade profile coordinates were generated using the Interactive Computational Aerodynamics Analysis Program (ICAAP) (10).

Airfoil Coordinate Point Data: (10)

Leading Edge Radius = 0.006408 inches

Trailing Edge Radius = 0

Table B.2. Airfoil Coordinate Point Data

X/Chord	Y/Chord	X/Chord	Y/Chord
1.00000000	0.00000000	0.97986622	0.00183903
0.93954295	0.00552218	0.89918085	0.00920888
0.84871563	0.01381840	0.79827892	0.01842531
0.71774530	0.02643880	0.63756397	0.03374672
0.55792706	0.03961975	0.47932911	0.04266958
0.40062962	0.04191747	0.35131688	0.04026729
0.30192772	0.03778660	0.25245675	0.03441011
0.20289458	0.03002248	0.15322449	0.02445792
0.10340541	0.01748430	0.08341242	0.01423035
0.06335589	0.01067336	0.04318934	0.00678953
0.02277440	0.00259732	0.01230437	0.00048655
0.00685249	-0.00043930	0.00202666	-0.00074084
0.00000000	0.00000000	-0.00002666	0.00228786
0.00314751	0.00663488	0.00769563	0.01057412
0.01722560	0.01684954	0.03681066	0.02669986
0.05664411	0.03474747	0.07658758	0.04170798
0.09659459	0.04783657	0.14677551	0.06085013
0.19710542	0.07112924	0.24754325	0.07923391
0.29807228	0.08537495	0.34868312	0.08961187
0.39937038	0.09190161	0.48067089	0.09118282
0.56207294	0.08390981	0.64243603	0.07182671
0.72225470	0.05689348	0.80172108	0.04036433
0.85128437	0.03027456	0.90081915	0.02019059
0.94045705	0.01212137	0.98013378	0.00404424
1.00000000	0.00000000		

Table B.3. Pressure Tap Coordinates

Suction Side		Pressure Side	
Tap #	% Surface Length	Tap #	% Surface Length
1	4.90	25	4.0
2	6.86	26	6.5
3	8.82	27	8.5
4	10.78	28	11.00
5	12.75	29	13.00
6	30.88	30	30.50
7	33.33	31	32.50
8	35.29	32	34.50
9	37.25	33	36.50
10	39.22	34	38.00
11	40.69	35	41.00
12	43.14	36	42.00
13	45.10	37	44.00
14	47.06	38	46.00
15	49.02	39	48.00
16	50.98	40	50.00
17	52.45	41	51.50
18	54.90	42	54.00
19	68.14	43	66.50
20	70.10	44	68.00
21	72.06	45	71.00
22	74.02	46	72.50
23	75.98	47	75.00
24	77.94	48	77.00

Blade and Cascade Geometrical Data

Chord = 2 inches
Span = 2 inches
Design Lift Coefficient = 0.9
Blade Thickness = 5.5%
Blade Spacing = 1.333 inches
Aspect Ratio (span-to-chord) = 1.0
Solidity (chord-to-spacing) = 1.5
Cascade Turning Angle = 31°

Incidence Angle = 0°
Blade Outlet Angle = 0°
Blade Camber Angle = 31°
Stagger Angle = 7.75°
Deflection Angle = 27.08°
Air Inlet Angle = 31°
Air Outlet Angle = 3.92°
Deviation Angle = 3.92°

Calculation of Deviation Angle

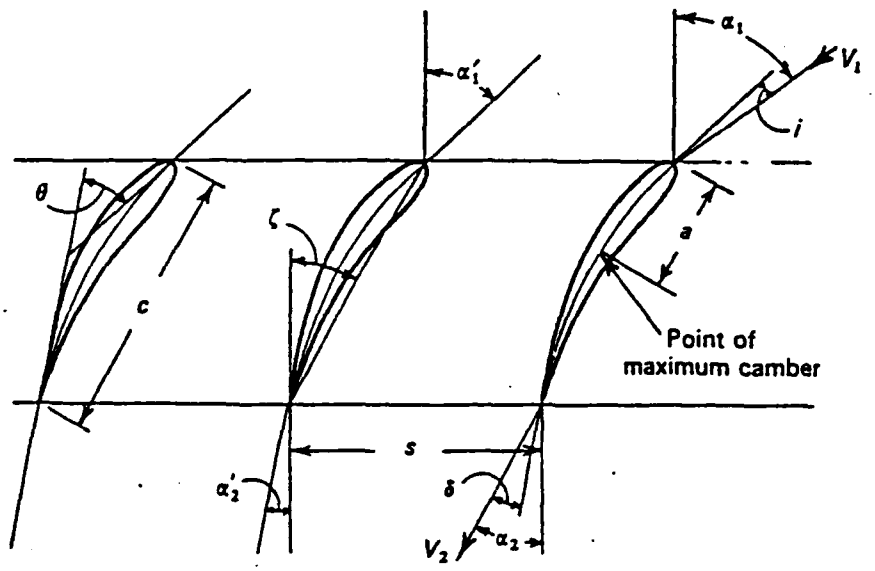

Figure B.1. Blade Geometry

Equation used: (5:192)

$$\delta = m\theta\sqrt{\frac{s}{c}} \qquad B-1$$

with:

$$m = 0.23\left(\frac{2a}{c}\right)^2 + 0.1\left(\frac{\alpha_2}{50}\right)$$

In our particular cascade, $\alpha_2' = 0$, therefore $\alpha_2 = \delta$ and equation B-1 can be rewritten as follows.

$$\delta = \left(.23\left(\frac{2a}{c}\right)^2 + .1\left(\frac{\delta}{50}\right)\right)\theta\sqrt{\frac{s}{c}} \qquad B-3$$

Rearranging and solving for δ gives

$$\delta = \frac{.23\left(\frac{2a}{c}\right)^2 \theta\sqrt{\frac{s}{c}}}{\left[1-\left(\frac{.1}{50}\right)\theta\sqrt{\frac{s}{c}}\right]} \qquad B-4$$

For the NACA 641905 blade, $\theta = 31°$, $s = 1.333''$, $c = 2.0''$, and a/c=0.4. Substitution yields

$$\delta = \frac{(.23)((2)(.4))^2(31)\sqrt{\frac{1.333}{2.0}}}{\left[1-\left(\frac{.1}{50}\right)(31)\sqrt{\frac{1.333}{2.0}}\right]} = 3.924° \qquad B-5$$

This is the predicted deviation angle based on the cascade geometry.

Blade Material

The cascade blades were molded using an epoxy resin manufactured by the Fiber-Resin Corporation. The following information is taken from the fact sheet on the epoxy material provided by the company.

Product: FR-44 Hi-Temp Casting Resin

Description:

Resin: FR-44 is a readily pourable epoxy for casting parts that require good strength to 300-400°F. The aluminum filler provides high thermal conductivity. FR-44 is available with a variety of hardeners for achieving the desired pot life and temperature resistance.

Hardener: Hardener 5595 was used for the cascade blades. It is a low-viscosity, non-staining and non-crystallizing material. It gels FR-44 in 20-30 minutes at 200°F.

Ratio by Weight: 100/7

Pot Life: 1.5 hours

Service Temperature: 350°F

Appendix C. *Pressure Transducer Calibration*

The pressure transducers used in this thesis investigation were calibrated assuming a linear relationship between pressure and voltage. The pressure transducers used to measure gage pressures at the test section inlet and the downstream measuring stations were calibrated using a 100 inch water manometer. In this procedure, the transducer was first exercised through its pressure range (0 to 55.36″ H_2O) using regulated 100 psig facility air. Voltages for 0″ H_2O (0 psig) and 55.36″ H_2O (2 psig) were recorded and a linear calibration curve calculated. The slope and intercept of this line were automatically compared to those of the previous calibration to check for excessive drift. The scanivalve system and the pressure transducer measuring the tank total pressure were calibrated in the same manner except they were exercised through a pressure range of 0″ H_2O to 69.2″ H_2O (2.5 psig).

Due to a tendency to drift, the scanivalve pressure transducer was continuously re-calibrated throughout the data collection process. This was done by leaving one scanivalve channel open to the atmosphere and monitoring the tank total pressure with a second scanivalve channel. The atmospheric and total tank pressures were assumed to be accurately known and a new linear two point calibration curve was determined for the scanivalve at the beginning of each series of data collection. To ensure the scanivalve was stepping through its channels correctly, every fifth scanivalve channel monitored a reference pressure of approximately 1.5 psig. No excessive scanivalve calibration drift or erroneous channel scanning was observed during this research project.

The pressure transducer used to measure atmospheric pressure was calibrated using a mercury manometer and a vacuum pump. The vacuum pump was used to draw a vacuum on the pressure transducer. The voltages corresponding to 0 psia and atmospheric pressure were measured and used to calculate coefficients assuming a linear calibration law. A wall-mounted vernier scale mercury barometer was used to determine the reference atmospheric pressure.

During calibration, all reference pressures were assumed to be accurately measured to 0.05 inch (one-half of one scale graduation).

Appendix D. *Hot Wire Calibration*

The fundamentals of hot wire anemometry are firmly rooted in the field of heat transfer. A hot wire anemometer utilizes the relationship between the rate of heat loss from a sensing element and the flow speed of its fluid environment. The sensing element, typically a platinum or tungsten wire (hot wire), or a nickel or platinum film on a glass substrate (hot film), is placed in the flow and heated to an elevated temperature. As the fluid flows past, the sensor dissipates heat. The faster the fluid velocity, the greater this heat dissipation. The amount of electrical input required from the anemometer to counterbalance this heat loss is correlated with the flow velocity and used to calibrate the sensing element. There are two major types of anemometers, the constant current type and the constant temperature type. Each uses this heat transfer phenomena, but in different ways. The constant current anemometer maintains a constant current through the wire and allows the wire temperature to vary with velocity. The constant temperature anemometer adjusts the voltage supplied to the sensor as needed to maintain a constant wire temperature (7:506). Since the constant temperature anemometer was used in this thesis effort, only its theory of operation will be discussed in detail.

Bradshaw (3:109) cites four ways heat is transferred from the sensor. They are radiation, buoyant convection, conduction to the wire supports, and forced convection. For the typical airflow velocities of this investigation (about 450 ft/s), radiation heat loss and buoyant convection can be neglected. This leaves conduction to the probe supports and forced convection as the two major contributors to sensor heat dissipation. In the following development of the applicable heat transfer equations, the heat loss is assumed to be due entirely to forced convection. Heat conduction to the probe supports is accounted for when determining the calibration constants A, B, and C. In a constant temperature anemometer the sensing element forms one leg of a wheatstone bridge circuit as shown schematically in Figure D.1 (19:15).

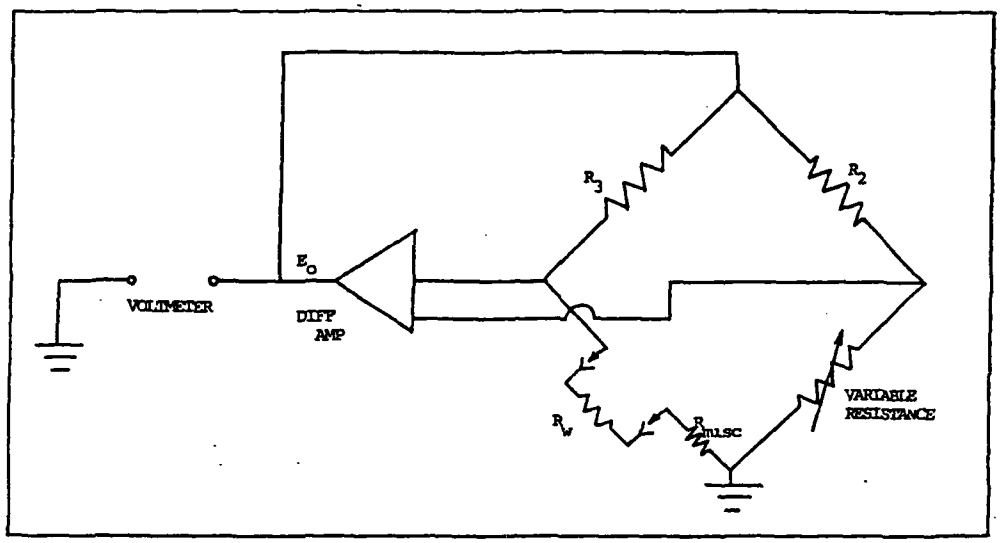

Figure D.1. Hot Wire Bridge Circuit

By regulating the amount of voltage supplied to the circuit, the anemometer can maintain a constant sensor resistance, thereby keeping the sensor at a desired operating temperature. The total circuit voltage is the sum of the voltages across resistor #3, the fifteen foot anemometer cables, the probe support and holder, and the voltage across the sensor and can be expressed as follows:

$$E_o = E_3 + E_w = I_w R_w + I_w R_3 + I_w R_{misc} = I_w (R_3 + R_w + R_{misc}) \qquad D-1$$

Rearranging this equation allows us to express sensor voltage in terms of the total circuit voltage and the individual resistances.

$$E_w = \frac{E_o R_w}{(R_3 + R_w + R_{misc})} \qquad D-2$$

At equilibrium, the power supplied to the sensor must equal the heat dissipated to the fluid. This relationship can be written as follows:

$$I_w{}^2 R_w = hA\left(T_w - T_{AW}\right) \qquad D-3$$

The voltage law $E = IR$ allows us to rewrite the equation for power supplied to the sensor in terms of the sensor's voltage and resistance.

$$R_w I_w^2 = R_w \left(\frac{E_w}{R_w}\right)^2 = \frac{E_w^2}{R_w} \qquad D-4$$

Replacing E_w in equation D-4 with equation D-2 and substituting that expression into the energy balance equation (equation D-3) yields (after some rearrangement)

$$h = \frac{E_o{}^2 R_w}{\left(R_3 + R_w + R_{misc}\right)^2 \pi dl \left(T_w - T_{AW}\right)} \qquad D-5$$

Dividing each side of equation D-5 by the fluid thermal conductivity, K, and multiplying through by the wire diameter, d, results in an expression for the Nusselt number, Nu.

$$Nu = \frac{hd}{K} = \frac{E_o{}^2 R_w}{K\left(R_3 + R_w + R_{misc}\right)^2 \pi l \left(T_w - T_{AW}\right)} \qquad D-6$$

Reynolds number is another quantity based on flow conditions. A typical expression for Reynolds number is as follows:

$$Re = \frac{\rho V d}{\mu} \qquad D-7$$

If a relationship between Nusselt number and Reynolds number is assumed, measured anemometer voltages can be correlated to fluid flow velocities.

Bradshaw (3:114) cites this relationship between Nusselt number and Reynolds number as the key bit of information needed by the hot wire anemometer system. One of the first semi-empirical relationships developed was $Nu = A + BRe^{0.5}$, known as Kings law (3:114). Later, Collis and Williams (6:370) determined that fluid property variation could be accounted for using a temperature loading factor. With $T_m \equiv 0.5(T_w + T_f)$, and a

temperature loading factor applied to the Nusselt number, they obtained the following equation:

$$Nu\left(\frac{T_m}{T_f}\right)^{-0.17} = A + BRe^n \qquad D-8$$

The applicable Reynolds number is indicated in Table D.1.

Table D.1. Reynolds Number Range (3:115)

	0.02 < Re < 44	44 < Re < 140
n	0.45	0.51
A	0.24	0.00
B	0.56	0.48

Another method of accounting for elevated temperatures when relating Nusselt numbers and Reynolds numbers allows the exponent in equation D-8 to be a calibration variable and results in a relationship of the form

$$Nu\left(\frac{T_m}{T_f}\right)^{b} = A + BRe^n \qquad D-9$$

Velocity effects on the airflow are included by using the Eckert reference temperature concept (10:268) and evaluating the fluid properties at a mean airflow temperature defined as follows:

$$T_m = \frac{T_w + T_f}{2} + 0.22\,(T_{AW} - T_f) \qquad D-10$$

The exponent n is selected based on the Reynolds number of the expected flow conditions using the same criteria employed by Collis and Williams (6:370). The constants A, B, b are found by applying a linear curve fit to a collection of data points taken over a wide range of temperatures and velocities. Iterations are performed on b, A, and B to find

the constant values which minimize the standard deviation for a given n. This method yields calibration curves of the type shown in Figure D.2 for an X-wire. This calibration procedure has been used on all previous thesis efforts performed in the AFIT Cascade Test Facility.

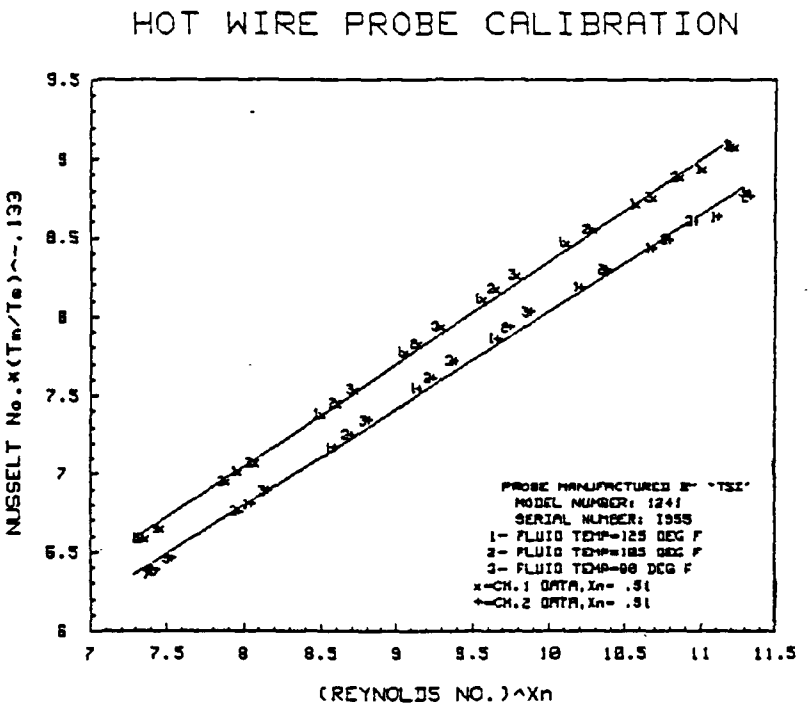

Figure D.2. Two-Term Correlation for Nusselt Number

To improve the accuracy of the calibration process, the Nusselt-Reynolds relationship was modelled as quadratic rather than linear. This results in the following equation.

$$Nu\left(\frac{T_m}{T_f}\right)^b = A + BRe^{0.5} + CRe \qquad D-11$$

An iteration scheme is used to find the constants A, B, C, and b which yield the parabolic curve fit with the minimum standard error of estimate through a set of calibration data collected over a wide range of temperatures and velocities. If an X-wire probe is used, each sensor is evaluated independently yielding two complete sets of constants. The resulting calibration curves are shown in Figure D.3. As can be seen, the data fit the three-term calibration law closely.

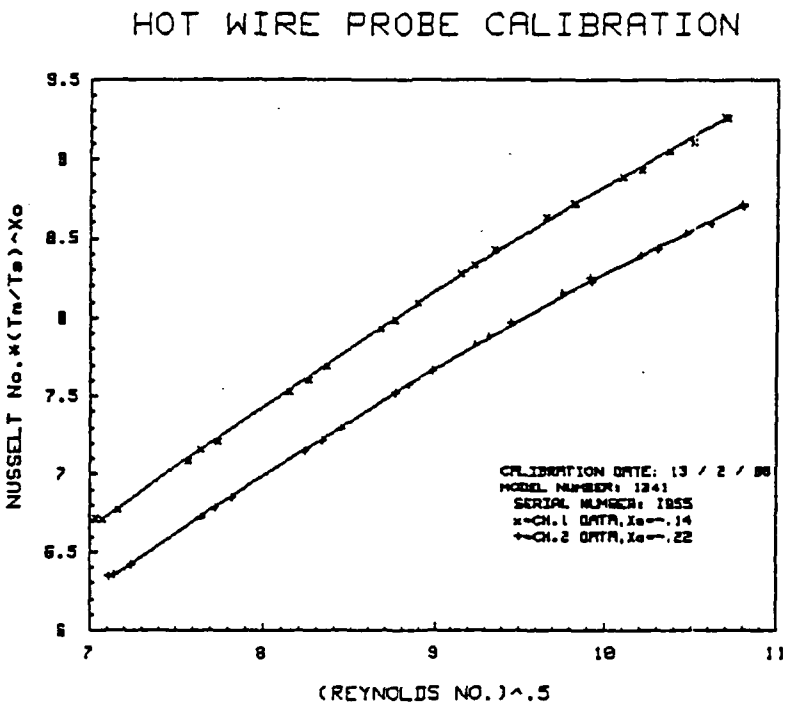

Figure D.3. Three-Term Correlation for Nusselt Number

The probe is calibrated using a modified TSI 1125 calibrator. Pressure transducers and thermocouples monitor the air passing through the calibrator, so both flow direction and flow velocity are known. A quartz heater and a set of hot and cold air regulator valves provide a temperature control capability. The probe is mounted in the calibrator as shown in Figure D.4 and the airflow is varied through a range of temperatures (90°F to 125°F) and velocities (300 ft/s to 650 ft/s). As temperature and velocity are varied, the changes in voltage across the hot film sensors are recorded.

The calibration procedure is divided into two major steps. The first determines sensor resistance variation with temperature. This is accomplished by placing the probe in a virtually static airflow of known temperature and measuring its sensors' cold resistances. Cold resistances are measured without energizing the sensors, so it is assumed the probe is in thermal equilibrium with its fluid environment. As air temperature is increased, sensor resistances are measured at three temperatures spanning the range of expected test conditions.

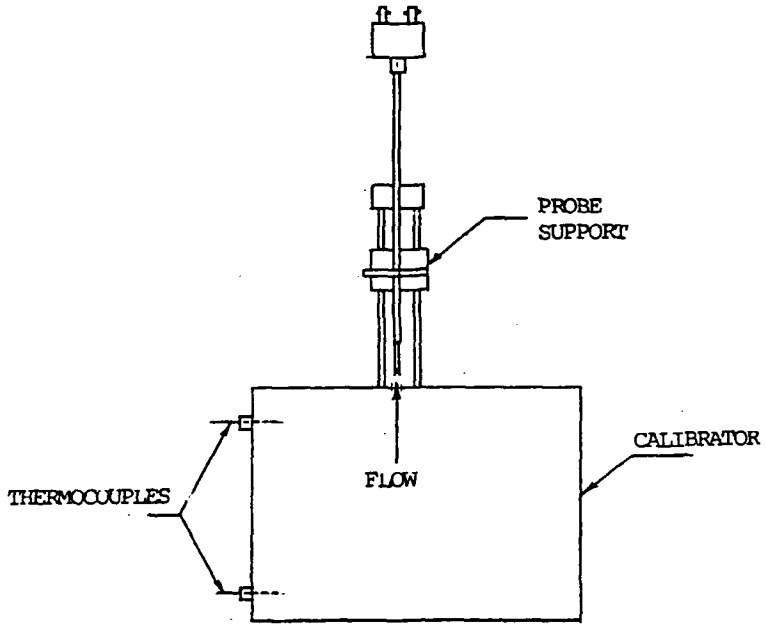

Figure D.4. Probe in Calibrator

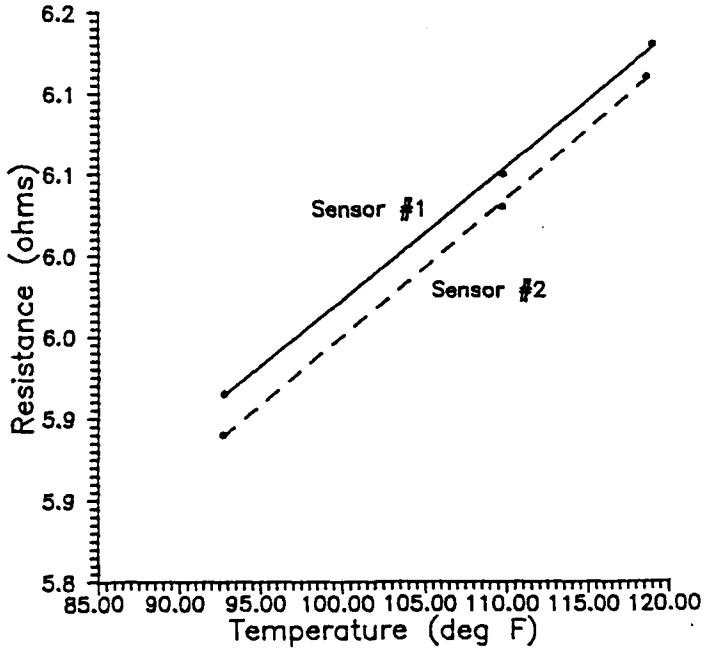

Figure D.5. Sensor Temperature-Resistance Relationship

The linearity of the relationship between temperature and resistance is shown in Figure D.5 in which a linear least square fit is applied to the sensor data. Extrapolation

of this line determines the resistance needed to keep the sensor at a chosen operating temperature of 482°F.

Another quantity that is of interest in the heat transfer phenomena between the sensor and its environment is the adiabatic wall temperature, T_{AW}, also known as the recovery temperature. This is the temperature attained by the sensor surface when no heat transfer is taking place. The adiabatic wall temperature for the expected test conditions is found by placing the probe in an airflow set to the expected test conditions and measuring the sensor resistance. Using the linear resistance-temperature relationship, the adiabatic wall temperature is found. The airflow's total temperature is measured in a static region of the flow field and its static temperature is determined using the relationship

$$T_f = T_o - \frac{V^2}{2C_p g_c J} \qquad D-12$$

Based on these values, the recovery factor, r_c, is calculated.

$$r_c = \frac{T_{AW} - T_f}{T_o - T_f} \qquad D-13$$

The recovery factor accounts for the fact that the fluid is brought to rest viscously in the boundary layer (11:267). Once determined, the recovery factor is used to calculate T_{AW} in varying flow conditions.

$$T_{AW} = (T_o - T_f)\, r_c + T_f \qquad D-14$$

After the operating resistance and the recovery factor for each sensor have been determined, the second portion of the calibration process begins. In this part the airflow velocity and temperature are varied over a wide range (typically 90°F-125°F and 250 ft/s to 650 ft/s). The voltage required to keep each sensor at its operating temperature is recorded. Equation D-6 is used to calculate the Nusselt number at each data point. Since probe geometry and flow velocities are known, the applicable Reynolds numbers can be calculated using the following equation.

$$Re = \frac{\rho U_{eff} d}{\mu} \qquad D-15$$

Details on determining velocities normal to the sensors can be found in Appendix E.

The properties of the flow, namely density, viscosity, and thermal conductivity are evaluated at the mean temperature defined by equation D-10. All three properties are temperature dependent and this fact must be reflected in their calculation. Equations D-16 through D-18 are used in the calibration process.

$$K = K_o \left(\frac{T_m}{T_o}\right)^{0.8} \qquad D-16$$

Sutherland's Law: (17:256-257)

$$\frac{\mu}{\mu_o} = \left(\frac{T_m}{T_o}\right)^{1.5} \left(\frac{T_o + S_1}{T + S_1}\right) \qquad D-17$$

Ideal gas law:

$$\rho = \frac{P}{RT_m} \qquad D-18$$

Once all of the data points have been taken in the desired temperature and velocity ranges the calibration constants A, B, C, and b are calculated for each sensor in the manner described earlier. These calibration curves are now ready to be used to reduce experimental data.

Appendix E. *Calculation of Velocity Components from X-wire Measurements*

Determining Velocity Components in Bisector Reference Frame

This development of the X and Y components of the mean velocity is based on an X-wire with wire angles $\neq 90°$.

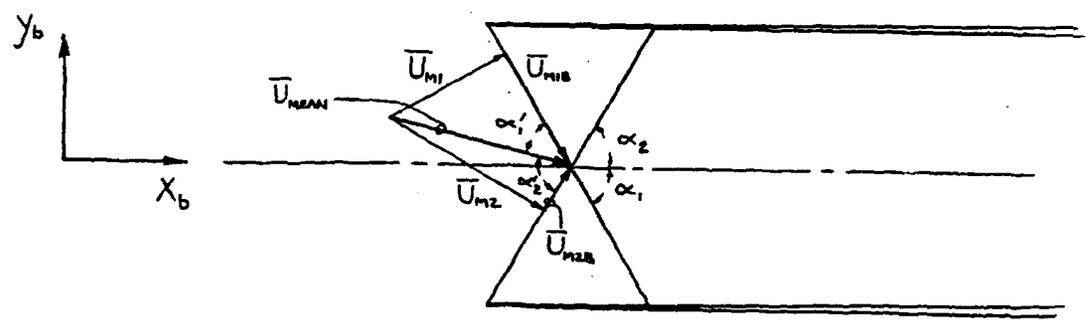

Figure E.1. Wire Geometry

Note: From definition of a bisector, $\alpha_1 = \alpha_2 = \alpha$.

From Figure E.1 we note

$$\overline{U}_{MEAN} = \overline{U}_{M1} + \overline{U}_{M1B} = \overline{U}_{M2} + \overline{U}_{M2B} \qquad E-1$$

$$\overline{U}_{MEAN} \neq \overline{U}_{M1} + \overline{U}_{M2} \quad \left(\text{for } 90° \text{ X} - \text{wire } \overline{\text{U}}_{\text{MEAN}} = \overline{\text{U}}_{\text{M1}} + \overline{\text{U}}_{\text{M2}}\right) \qquad E-2$$

$$\sin \alpha_1' = \frac{\overline{U}_{M1}}{\overline{U}_{MEAN}} \qquad E-3$$

$$\sin \alpha_2{}' = \frac{\overline{U}_{M2}}{\overline{U}_{MEAN}} \qquad E-4$$

$$\alpha_2{}' = 2\alpha - \alpha_1{}' \qquad E-5$$

The following values in Figure E.1 are known:

1) $|U_{M1}|$, $|U_{M2}|$ From hot wire calibration

2) $\alpha_2 = \alpha_1 = \alpha$ From angle measurement of X-wire

Divide equation E-4 by E-3.

$$\frac{\sin \alpha_2{}'}{\sin \alpha_1{}'} = \frac{\overline{U}_{M2}}{\overline{U}_{M1}} \qquad E-6$$

Substituting equation E-5 into E-6 and solving for $\alpha_1{}'$ yields (after some rearrangement)

$$\alpha_1{}' = \arctan \left[\frac{\overline{U}_{M1} \sin 2\alpha}{\left(\overline{U}_{M2} + \overline{U}_{M1} \cos 2\alpha \right)} \right] \qquad E-7$$

Once $\alpha_1{}'$ is known, $\alpha_2{}'$ can be found using $\alpha_2{}' = 2\alpha - \alpha_1{}'$.

The direction and magnitude of U_{MEAN} can now be found.

$$|U_{MEAN}| = \frac{|U_{M1}|}{\sin \alpha_1{}'} \qquad E-8$$

$$U_{MEAN_X} = |U_{MEAN}| \cos \left(\alpha_2{}' - \alpha \right) \qquad E-9$$

$$U_{MEAN_Y} = |U_{MEAN}| \sin \left(\alpha_2{}' - \alpha \right) \qquad E-10$$

Note: This mean velocity is given in terms of the probe bisector coordinate axis. No correction has been made for probe skewness or skewness between the probe support and the cascade reference frame. Eventually, all of the velocities need to be given in terms of the cascade reference frame.

Converting from Probe Bisector Coordinates to Test Section Coordinates

$\overline{U}_{MEAN}$ has been calculated in terms of the sensor bisector reference frame. Since the sensor bisector may not be parallel to the probe support centerline (due to probe skewness), the velocities need to be converted from the sensor bisector reference frame (X_B Y_B, see Figure E.2) to the probe support reference frame (X_{PS} Y_{PS}). By aligning the probe support with the test section reference frame, the velocities can be found in terms of the fixed test section reference frame (X_{TS} Y_{TS}, see Figure E.3).

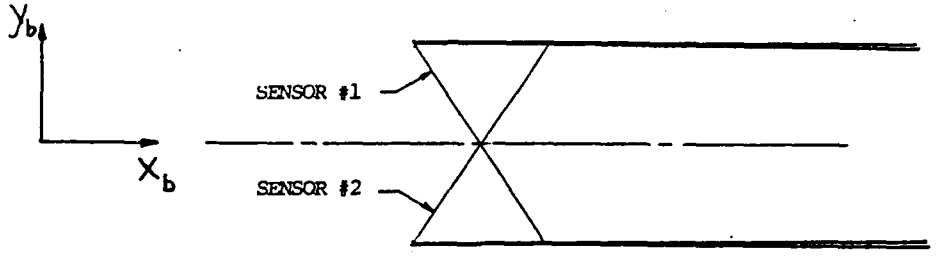

Figure E.2. Bisector Reference Frame

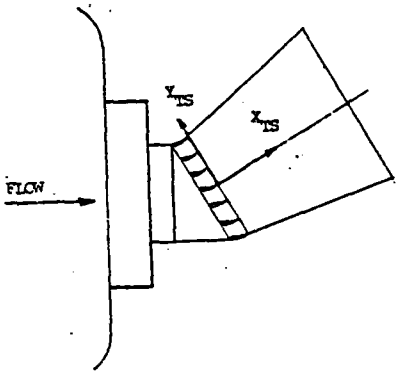

Figure E.3. Test Section Reference Frame

Assumptions

1) X_{TS} and Y_{TS} are fixed by the test section orientation.

2) Tailboards are adjusted to give uniform flow with respect to the X_{TS} and Y_{TS} reference frame.

3) The probe support is oriented to align with the X_{TS} and Y_{TS} reference frame.

4) Velocities are first found with respect to the sensor bisector reference frame (X_B Y_B) and then converted to the test section reference frame (X_{TS} Y_{TS}).

5) The measured offset angle, $\theta/2$, is used to convert probe sensor velocities to test section velocities.

6) Sign convention for θ:

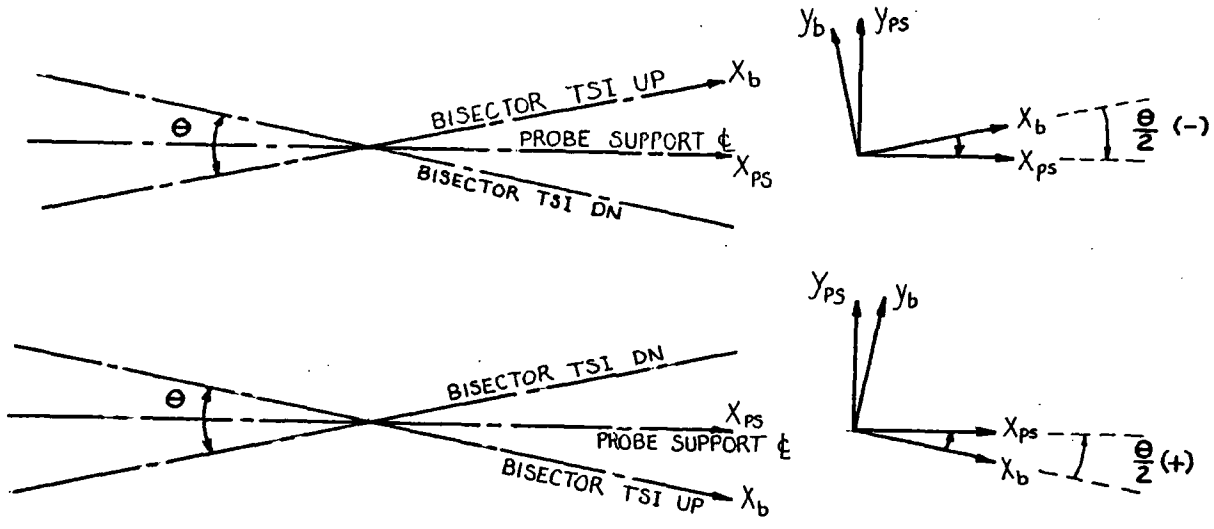

Figure E.4. Sensor Sign Convention

The TSI logo is stamped on one side of the X-wire probe. TSI UP refers to the sensor bisector orientation to the probe support centerline when this TSI logo faces upward. TSI DN refers to the sensor bisector orientation to the probe support centerline when the probe has been rotated axially 180° (TSI logo facing downward).

7) The direction cosine matrix is

$$\begin{bmatrix} X_{PS} \\ Y_{PS} \end{bmatrix} = \begin{bmatrix} \cos\left(\frac{\theta}{2}\right) & \sin\left(\frac{\theta}{2}\right) \\ -\sin\left(\frac{\theta}{2}\right) & \cos\left(\frac{\theta}{2}\right) \end{bmatrix} \begin{bmatrix} X_B \\ Y_B \end{bmatrix} \qquad E-11$$

so X_{PS} and Y_{PS} can be written as

$$X_{PS} = X_B \cos\left(\frac{\theta}{2}\right) + Y_B \sin\left(\frac{\theta}{2}\right) \qquad E-12$$

$$Y_{PS} = -X_B \sin\left(\frac{\theta}{2}\right) + Y_B \cos\left(\frac{\theta}{2}\right) \qquad E-13$$

8) As long as the probe support is correctly aligned, $X_{TS} = X_{PS}$ and $Y_{TS} = Y_{PS}$.

Determining the Sensor's Normal Component of Velocity During Probe Calibration

When the X-wire probe is mounted in the TSI 1125 calibrator the direction of the flow is assumed to be parallel to the centerline of the probe support. Any skewness between the centerline of the probe support and the probe bisector is measured ($\theta/2$) and corrected in the calculations. The angle between the two sensors (2α) is also measured. See Figures E.5 and E.6 for the schematic of this layout.

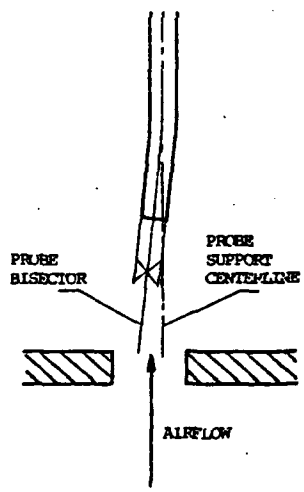

Figure E.5. Probe/Calibrator Orientation

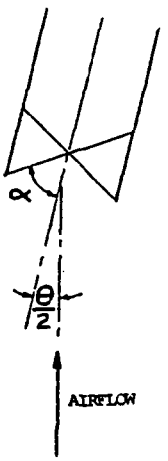

Figure E.6. Probe Orientation

The components of the velocity perpendicular to each sensor (U_{eff}) are as follows (See Figure E.7):

$$U_{eff}(1) = V_{cal} \sin(\alpha + \theta) \qquad E - 14$$

$$U_{eff}(2) = V_{cal} \sin(\alpha - \theta) \qquad E - 15$$

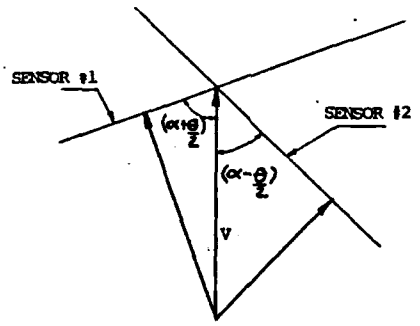

Figure E.7. Velocity Components With Respect to Sensors

Appendix F. *Turbulence Measurements*

The equation used to quantify the relative level of turbulence in a stream of average velocity V is given by Cebeci (4:13).

$$\sigma = \frac{1}{|V|}\sqrt{\frac{\overline{u^2} + \overline{v^2} + \overline{w^2}}{3}} \qquad F-1$$

For two-dimensional cascade flow this equation reduces to

$$\sigma = \frac{1}{|V|}\sqrt{\frac{\overline{u^2} + \overline{v^2}}{2}} \qquad F-2$$

The hot-film X-wire is placed in the flowfield and each sensor takes an AC root mean square (rms) reading (e_{rms}) reflecting the velocity fluctuations perpendicular to the sensor and a DC voltage reading (E) corresponding to the perpendicular flow velocity. Relating these voltage values to the established hot wire calibration law results in an equation expressing the rms velocity fluctuation perpendicular to the wire. Once this value is known for each sensor, knowledge of the wire geometry can be used to derive an equation for the X and Y components of turbulence. With this, the relative level of turbulence for the flow can be calculated. The following derivations outline this procedure.

Part One

Basic Premises:

a) Each sensor takes an AC rms reading.

b) This reading (e_{rms}) applies to the flow perpendicular to the sensor.

c) The mean velocity perpendicular to the sensor (U_{eff}) and its corresponding voltage (E) are known.

d) The calibration curves are based on mean voltages and mean velocities.

$$K_1\left(E^2\right) = A + BK_2{U_{eff}}^{0.5} + CK_3U_{eff} \qquad F-3$$

e) A, B, and C are constants.

f) $K_1 = R_w/[\mathrm{K}(R_3 + R_w + R_{misc})^2\pi l(T_w - T_{AW})]$, $K_2 = (\rho d/\mu)^{0.5}$, and $K_3 = \rho d/\mu$.

Derivation

1) Take the derivative of both sides of the calibration law:

$$2K_1 E\, dE = \left[\frac{BK_2}{2U_{eff}{}^{0.5}} + CK_3\right] dU_{eff} \qquad F-4$$

2) dE and dU_{eff} are fluctuations. Therefore, $dE = e'$, $dU_{eff} = u'$, and

$$2K_1 E e' = \left[\frac{BK_2}{2U_{eff}{}^{0.5}} + CK_3\right] u' \qquad F-5$$

3) Square both sides to get

$$4K_1{}^2E^2e'^2 = \left[\frac{BK_2}{2U_{eff}{}^{0.5}} + CK_3\right]^2 u'^2 \qquad F-6$$

and rewrite to obtain

$$4K_1{}^2E^2e'^2 = \left[\frac{B^2K_2{}^2}{4U_{eff}} + \frac{BCK_2K_3}{U_{eff}{}^{0.5}} + C^2K_3{}^2\right] u'^2 \qquad F-7$$

4) Take the mean time average of both sides

$$4K_1{}^2E^2e_{rms}{}^2 = \left[\frac{B^2K_2{}^2}{4U_{eff}} + \frac{BCK_2K_3}{U_{eff}^{0.5}} + C^2K_3{}^2\right] u_{rms}{}^2 \qquad F-8$$

and solve for u_{rms}:

$$u_{rms} = \frac{4K_1 E\, e_{rms} U_{eff}}{\sqrt{B^2K_2{}^2U_{eff} + 4BCK_2K_3U_{eff}{}^{1.5} + 4C^2K_3{}^2U_{eff}{}^2}} \qquad F-9$$

Everything except u_{rms} is known, so equation F-9 can be used to calculate u_{rms}.

Part Two

Develop the equations for the X_B and Y_B components of velocity in terms of the effective velocities perpendicular to the sensors of the X-wire probe. This development is relative to a coordinate system based on the X-wire bisector.

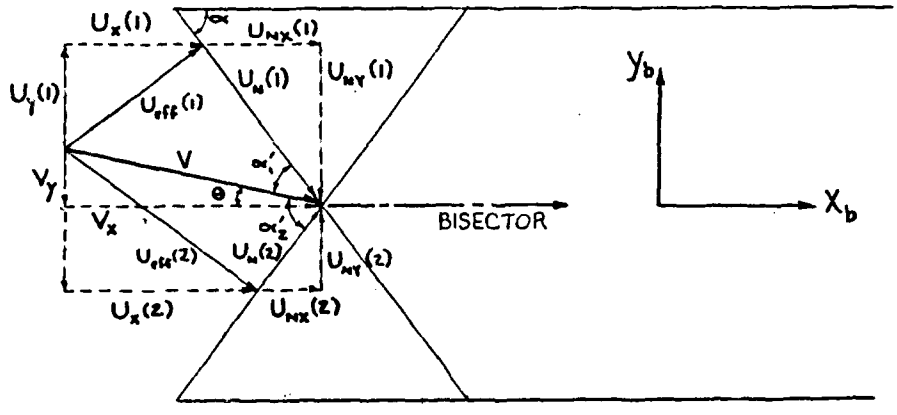

Figure F.1. Velocity Vector Components

Using Figure F.1 and trigonometry, the following equations can be written.

$$V_X = U_X(1) + U_{NX}(1) \quad \text{(sensor \#1)} \qquad F-10a$$

$$V_X = U_X(2) + U_{NX}(2) \quad \text{(sensor \#2)} \qquad F-10b$$

$$V_Y = U_{NY}(1) - U_Y(1) \quad \text{(sensor \#1)} \qquad F-11a$$

$$V_Y = U_Y(2) - U_{NY}(2) \quad \text{(sensor \#2)} \qquad F-11b$$

$$U_X(1) = U_{eff}(1)\sin\alpha \qquad F-12a$$

$$U_X(2) = U_{eff}(2)\sin\alpha \qquad F-12b$$

$$U_N(1) = U_{eff}(1)\left(\frac{\cos\alpha_1'}{\sin\alpha_1'}\right) \qquad F-12c$$

$$U_N(2) = U_{eff}(2)\left(\frac{\cos\alpha_2'}{\sin\alpha_2'}\right) \qquad F-12d$$

$$U_{NX}(1) = U_N(1)\cos\alpha = U_{eff}(1)\left(\frac{\cos\alpha_1'}{\sin\alpha_1'}\right)\cos\alpha \qquad F-12e$$

$$U_{NX}(2) = U_N(2)\cos\alpha = U_{eff}(2)\left(\frac{\cos\alpha_2'}{\sin\alpha_2'}\right)\cos\alpha \qquad F-12f$$

$$U_Y(1) = U_{eff}(1)\cos\alpha \qquad F-12g$$

$$U_Y(2) = U_{eff}(2)\cos\alpha \qquad F-12h$$

$$U_{NY}(1) = U_N(1)\sin\alpha = U_{eff}(1)\left(\frac{\cos\alpha_1'}{\sin\alpha_1'}\right)\sin\alpha \qquad F-12i$$

$$U_{NY}(2) = U_N(2)\sin\alpha = U_{eff}(2)\left(\frac{\cos\alpha_2'}{\sin\alpha_2'}\right)\sin\alpha \qquad F-12j$$

$$V_X = U_{eff}(1)\left[\sin\alpha + \left(\frac{\cos\alpha_1'}{\sin\alpha_1'}\right)\cos\alpha\right] \qquad F-13$$

$$V_X = U_{eff}(2)\left[\sin\alpha + \left(\frac{\cos\alpha_2'}{\sin\alpha_2'}\right)\cos\alpha\right] \qquad F-14$$

$$V_Y = U_{eff}(1)\left[\left(\frac{\cos\alpha_1'}{\sin\alpha_1'}\right)\sin\alpha - \cos\alpha\right] \qquad F-15$$

$$V_Y = U_{eff}(2)\left[\cos\alpha - \left(\frac{\cos\alpha_2'}{\sin\alpha_2'}\right)\sin\alpha\right] \qquad F-16$$

Solve equations F-13 and F-15 for $(\cos\alpha_1'/\sin\alpha_1')$.

$$\frac{\cos\alpha_1'}{\sin\alpha_1'} = \frac{V_X - U_{eff}(1)\sin\alpha}{U_{eff}(1)\cos\alpha} \qquad F-17$$

$$\frac{\cos\alpha_1'}{\sin\alpha_1'} = \frac{V_Y + U_{eff}(1)\cos\alpha}{U_{eff}(1)\sin\alpha} \qquad F-18$$

Setting equation F-17 equal to F-18, solving for V_X, and simplifying gives

$$V_X = \frac{U_{eff}(1) + V_Y\cos\alpha}{\sin\alpha} \qquad F-19$$

Solve equations F-14 and F-16 for $(\cos\alpha_2'/\sin\alpha_2')$.

$$\frac{\cos\alpha_2'}{\sin\alpha_2'} = \frac{V_X - U_{eff}(2)\sin\alpha}{U_{eff}(2)\cos\alpha} \qquad F-20$$

$$\frac{\cos\alpha_2'}{\sin\alpha_2'} = \frac{U_{eff}(2)\cos\alpha - V_Y}{U_{eff}(2)\sin\alpha} \qquad F-21$$

Setting equation F-20 equal to F-21, solving for V_X, and simplifying gives

$$V_X = \frac{U_{eff}(2) - V_Y\cos\alpha}{\sin\alpha} \qquad F-22$$

Setting equation F-19 equal to equation F-22 results in the following equation for V_Y:

$$V_Y = \frac{U_{eff}(2) - U_{eff}(1)}{2\cos\alpha} \qquad F-23$$

V_X is obtained by substituting equation F-23 into equation F-19:

$$V_X = \frac{U_{eff}(1) + U_{eff}(2)}{2\sin\alpha} \qquad F-24$$

Part Three

Equations F-23 and F-24 relate V_X, V_Y, $U_{eff}(1)$, and $U_{eff}(2)$. But V_X and V_Y are velocities measured relative to the bisector reference frame, which may or may not be lined up with the probe support reference frame. $\theta/2$ is the angle between the probe bisector and the probe support centerline. See Appendix E for sign convention when designating $\theta/2$. Also, the probe support may not be aligned with the test section reference frame. The angle between the centerline of the probe support X_{PS} and the X-axis of the test section X_{TS} is given by β. The total angle offset of the probe bisector and the test section X-direction is the angle $[(\theta/2) + \beta]$. α is the angle between the two sensors. Therefore,

$$V_{X_{TS}} = V_X \cos\left(\frac{\theta}{2} + \beta\right) + V_Y \sin\left(\frac{\theta}{2} + \beta\right) \qquad F-25$$

$$V_{Y_{TS}} = -V_X \sin\left(\frac{\theta}{2} + \beta\right) + V_Y \cos\left(\frac{\theta}{2} + \beta\right) \qquad F-26$$

Let

$$\gamma = \left(\frac{\theta}{2} + \beta\right) \qquad F-27$$

Using equation F-27, substitute equations F-23 and F-24 into equations F-25 and F-26:

$$V_{X_{TS}} = \frac{\cos\gamma}{2\sin\alpha}\left(U_{eff}(1) + U_{eff}(2)\right) + \frac{\sin\gamma}{2\cos\alpha}\left(U_{eff}(2) - U_{eff}(1)\right) \qquad F-28$$

$$V_{Y_{TS}} = \frac{\cos\gamma}{2\cos\alpha}\left(U_{eff}(2) - U_{eff}(1)\right) - \frac{\sin\gamma}{2\sin\alpha}\left(U_{eff}(1) + U_{eff}(2)\right) \qquad F-29$$

Equations F-28 and F-29 can be simplified to obtain

$$V_{X_{TS}} = \frac{\cos(\alpha+\gamma)}{\sin 2\alpha} U_{eff}(1) + \frac{\cos(\alpha-\gamma)}{\sin 2\alpha} U_{eff}(2) \qquad F-30$$

$$V_{Y_{TS}} = \frac{\sin(\alpha-\gamma)}{\sin 2\alpha} U_{eff}(2) - \frac{\sin(\alpha+\gamma)}{\sin 2\alpha} U_{eff}(1) \qquad F-31$$

Differentiate equations F-30 and F-31 keeping in mind that α, and γ are constants.

$$dV_{X_{TS}} = \frac{\cos(\alpha+\gamma)}{\sin 2\alpha} dU_{eff}(1) + \frac{\cos(\alpha-\gamma)}{\sin 2\alpha} dU_{eff}(2) \qquad F-32$$

$$dV_{Y_{TS}} = \frac{\sin(\alpha-\gamma)}{\sin 2\alpha} dU_{eff}(2) - \frac{\sin(\alpha+\gamma)}{\sin 2\alpha} dU_{eff}(1) \qquad F-33$$

Square equations F-32 and F-33.

$$(dV_{X_{TS}})^2 = \frac{\cos^2(\alpha+\gamma)}{\sin^2 2\alpha} (dU_{eff}(1))^2 + \frac{\cos^2(\alpha-\gamma)}{\sin^2 2\alpha} (dU_{eff}(2))^2$$

$$+ \frac{2\cos(\alpha+\gamma)\cos(\alpha-\gamma)\, dU_{eff}(1)\, dU_{eff}(2)}{\sin^2 2\alpha} \qquad F-34$$

$$(dV_{Y_{TS}})^2 = \frac{\sin^2(\alpha-\gamma)}{\sin^2 2\alpha} (dU_{eff}(2))^2 + \frac{\sin^2(\alpha+\gamma)}{\sin^2 2\alpha} (dU_{eff}(2))^2$$

$$- \frac{2\sin(\alpha-\gamma)\sin(\alpha+\gamma)\, dU_{eff}(1)\, dU_{eff}(2)}{\sin^2 2\alpha} \qquad F-35$$

We want to add $dV_{X_{TS}}^2$ and $dV_{Y_{TS}}^2$ together in such a way as to get the $dU_{eff}(1)\, dU_{eff}(2)$ terms to cancel. Look at

$$A \equiv \cos(\alpha+\gamma)\cos(\alpha-\gamma) = (\cos\alpha\cos\gamma)^2 - (\sin\alpha\sin\gamma)^2 \qquad F-36$$

$$B \equiv \sin(\alpha+\gamma)\sin(\alpha-\gamma) = (\sin\alpha\cos\gamma)^2 - (\cos\alpha\sin\gamma)^2 \qquad F-37$$

Multiply equation F-34 by B and equation F-35 by A.

$$B(dV_{X_{TS}})^2 = \frac{B\cos^2(\alpha+\gamma)}{\sin^2 2\alpha} (dU_{eff}(1))^2 + \frac{B\cos^2(\alpha-\gamma)}{\sin^2 2\alpha} (dU_{eff}(2))^2$$

$$+ \frac{2AB}{\sin^2 2\alpha} dU_{eff}(1)\, dU_{eff}(2) \qquad F-38$$

$$A\,(dV_{Y_{TS}})^2 = \frac{A\sin^2(\alpha-\gamma)}{\sin^2 2\alpha}\,(dU_{eff}(2))^2 + \frac{A\sin^2(\alpha+\gamma)}{\sin^2 2\alpha}\,(dU_{eff}(1))^2$$

$$- \frac{2BA}{\sin^2 2\alpha} dU_{eff}(1)\, dU_{eff}(2) \qquad F-39$$

Add equations F-38 and F-39 together and take the time mean average.

$$B\,(u_{TS})^2 + A\,(v_{TS})^2 = \frac{B\cos^2(\alpha+\gamma)}{\sin^2 2\alpha}\,(u_{rms}(1))^2 + \frac{B\cos^2(\alpha-\gamma)}{\sin^2 2\alpha}\,(u_{rms}(2))^2$$

$$+ \frac{A\sin^2(\alpha-\gamma)}{\sin^2 2\alpha}\,(u_{rms}(2))^2 + \frac{A\sin^2(\alpha+\gamma)}{\sin^2 2\alpha}\,(u_{rms}(1))^2 \qquad F-40$$

Let

$$C = \frac{A}{B} \qquad F-41$$

Divide equation F-40 by B and rearrange (use F-41 to simplify notation):

$$(u_{TS})^2 + C\,(v_{TS})^2 = \frac{[\cos^2(\alpha+\gamma) + C\sin^2(\alpha+\gamma)]}{\sin^2 2\alpha}\,(u_{rms}(1))^2$$

$$+ \frac{[\cos^2(\alpha-\gamma) + C\sin^2(\alpha-\gamma)]}{\sin^2 2\alpha}\,(u_{rms}(2))^2 \qquad F-42$$

The equation for turbulence is

$$T_u = \frac{1}{|V| \sin 2\alpha} \sqrt{\frac{\left[\cos^2(\beta_1) + C \sin^2(\beta_1)\right] (u_{rms}(1))^2 + \left[\cos^2(\beta_2) + C \sin^2(\beta_2)\right] (u_{rms}(2))^2}{2}} \qquad F-43$$

where

$$\beta_1 = \alpha + \gamma \qquad F-44$$

and

$$\beta_2 = \alpha - \gamma \qquad F-45$$

Note: If the X-wire is a perfect 90° wire ($\alpha = 90$), then C=1 and the expression is exact for relative turbulence. If $\alpha \neq 90$, then equation F-43 will yield an answer either slightly higher or slightly lower depending on whether A/B or B/A is used when combining equations F-34 and F-35.

Appendix G. *Supplemental Flow Figures*

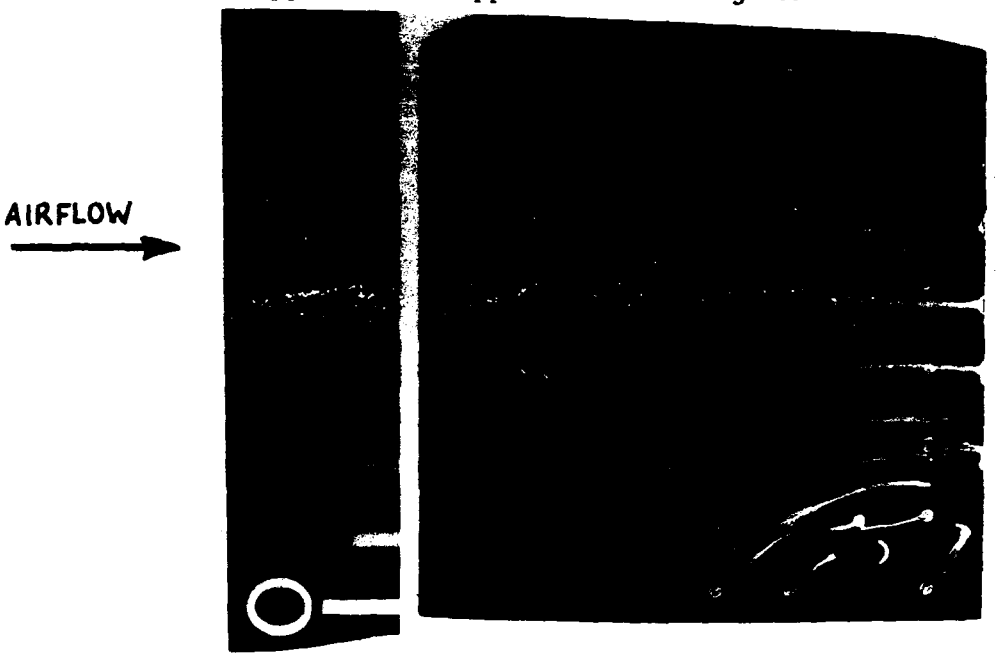

Figure G.1. Flow Pattern - Suction Side - Sidewall Suction Applied (Blade #2)

Figure G.2. Flow Pattern - Suction Side - Sidewall Suction Applied (Blade #4)

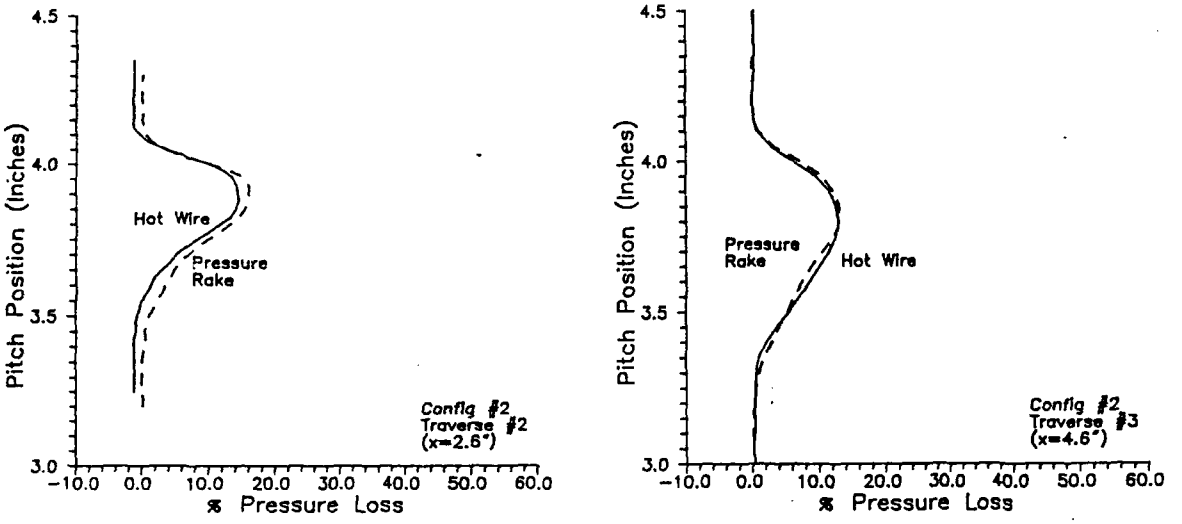

Figure G.3. Configuration #2 Pressure Profiles

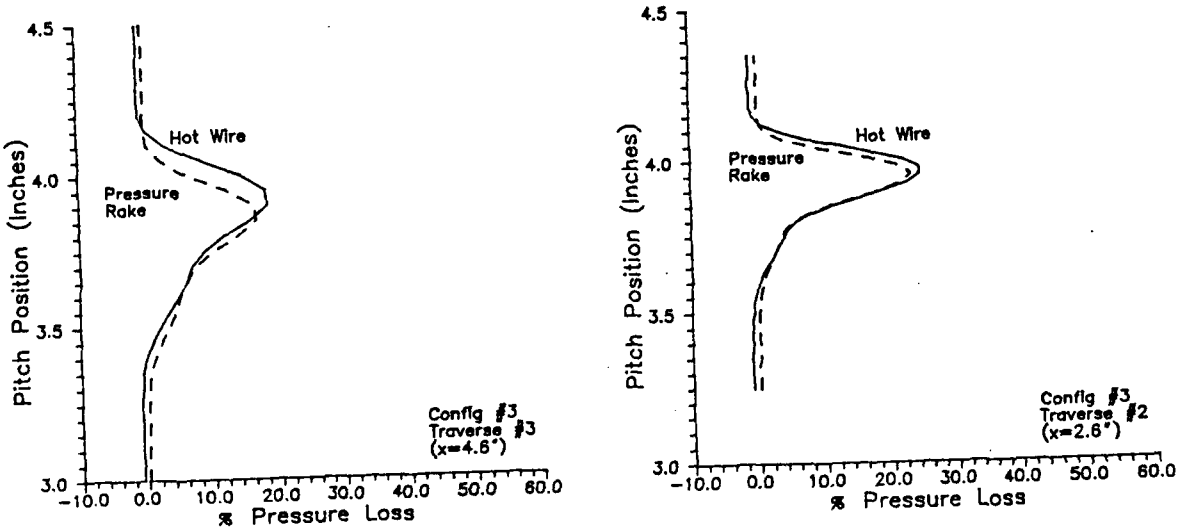

Figure G.4. Configuration #3 Pressure Profiles

Vita

Lieutenant Janet Lyle Veesart [redacted]

she attended Washington State University. In 1985 she graduated with a Bachelor of Science in Mechanical Engineering. A ROTC distinguished graduate, she received a Regular commission and was assigned to the Air Force Wright Aeronautical Laboratories at Wright-Patterson Air Force Base. Upon her arrival in Ohio, she began working in the Aero-Propulsion Laboratory's Turbine Engine Division as a project engineer involved with various advanced technology demonstrator engine programs.

Lieutenant Veesart began attending the Air Force Institute of Technology in 1986 on a part-time basis. In June 1988, she entered the School of Engineering as a full time student to complete the masters program in Aeronautical Engineering.

[redacted]

SECURITY CLASSIFICATION OF THIS PAGE

REPORT DOCUMENTATION PAGE

Form Approved
OMB No. 0704-0188

1a. REPORT SECURITY CLASSIFICATION: UNCLASSIFIED	1b. RESTRICTIVE MARKINGS
2a. SECURITY CLASSIFICATION AUTHORITY	3. DISTRIBUTION/AVAILABILITY OF REPORT
2b. DECLASSIFICATION/DOWNGRADING SCHEDULE	
4. PERFORMING ORGANIZATION REPORT NUMBER(S): AFIT/GAE/ENY/89J-3	5. MONITORING ORGANIZATION REPORT NUMBER(S)
6a. NAME OF PERFORMING ORGANIZATION: School of Engineering; 6b. OFFICE SYMBOL (If applicable): AFIT/ENY	7a. NAME OF MONITORING ORGANIZATION
6c. ADDRESS (City, State, and ZIP Code): Air Force Institute of Technology, Wright-Patterson AFB, Ohio 45433-6583	7b. ADDRESS (City, State, and ZIP Code)
8a. NAME OF FUNDING/SPONSORING ORGANIZATION; 8b. OFFICE SYMBOL (If applicable)	9. PROCUREMENT INSTRUMENT IDENTIFICATION NUMBER
8c. ADDRESS (City, State, and ZIP Code)	10. SOURCE OF FUNDING NUMBERS: PROGRAM ELEMENT NO. / PROJECT NO. / TASK NO. / WORK UNIT ACCESSION NO.

11. TITLE (Include Security Classification): See Block 19

12. PERSONAL AUTHOR(S): Janet Lyle Veesart, 1 Lt, United States Air Force

13a. TYPE OF REPORT	13b. TIME COVERED	14. DATE OF REPORT (Year, Month, Day)	15. PAGE COUNT
Thesis	FROM _____ TO _____	1989 June	

16. SUPPLEMENTARY NOTATION: form 14

17. COSATI CODES			18. SUBJECT TERMS (Continue on reverse if necessary and identify by block number)
FIELD	GROUP	SUB-GROUP	Cascade Testing, Crenulations, Compressor Blade, Wakes, Boundary Layer, Theses.
21	05		

19. ABSTRACT (Continue on reverse if necessary and identify by block number)

Title: Wake Dissipation and Total Pressure Loss in a Two-Dimensional Compressor Cascade With Crenulated Trailing Edges (U)

Thesis Advisor: Lt Col Paul I. King
Assistant Professor of Aerospace Engineering

Abstract: See other side

20. DISTRIBUTION/AVAILABILITY OF ABSTRACT: ☒ UNCLASSIFIED/UNLIMITED ☐ SAME AS RPT. ☐ DTIC USERS	21. ABSTRACT SECURITY CLASSIFICATION: UNCLASSIFIED
22a. NAME OF RESPONSIBLE INDIVIDUAL: Lt Col Paul I. King	22b. TELEPHONE (Include Area Code): 513-255-2362 / 22c. OFFICE SYMBOL: AFIT/ENY

DD Form 1473, JUN 86 — Previous editions are obsolete. — SECURITY CLASSIFICATION OF THIS PAGE

UNCLASSIFIED

Wake dissipation and total pressure loss in a two-dimensional, subsonic, compressor cascade with crenulated trailing edges were investigated in the Air Force Institute of Technology Cascade Test Facility. Three blade configurations, a baseline NACA 64-905 airfoil and two crenulated edge patterns were used. Hot wire anemometry and a total pressure rake were used to collect the flow data. The smaller crenulation configuration exhibited the greatest turning angle and the least total pressure losses. The most rapid wake dissipation was generated by the larger crenulations' counterrotating vortices accompanied by slightly higher pressure losses than those created by the small crenulations. Both crenulated blade configurations had better wake dissipation, increased turning angles, and smaller pressure loss coefficients than the uncrenulated baseline blade.